J. Fluid Mech. (2009), *vol.* 621, *pp.* 289–320.
doi:10.1017/S0022112008004953 Printed in the United Kingdom

Human sperm accumulation near surfaces: a simulation study

D. J. SMITH[1,2,3]†, E. A. GAFFNEY[3,4], J. R. BLAKE[1,3] AND J. C. KIRKMAN-BROWN[2,3]

[1]School of Mathematics and [2]Reproductive Biology and Genetics, College of Medicine, Dentistry and Health Sciences, University of Birmingham, Edgbaston, Birmingham B15 2TT, UK

[3]Centre for Human Reproductive Science, Birmingham Women's NHS Foundation Trust, Metchley Park Road, Edgbaston, Birmingham B15 2TG, UK

[4]Centre for Mathematical Biology, Mathematical Institute, University of Oxford, 24-29 St Giles', Oxford OX1 3LB, UK

(Received 24 April 2008 and in revised form 29 October 2008)

A hybrid boundary integral/slender body algorithm for modelling flagellar cell motility is presented. The algorithm uses the boundary element method to represent the 'wedge-shaped' head of the human sperm cell and a slender body theory representation of the flagellum. The head morphology is specified carefully due to its significant effect on the force and torque balance and hence movement of the free-swimming cell. The technique is used to investigate the mechanisms for the accumulation of human spermatozoa near surfaces. Sperm swimming in an infinite fluid, and near a plane boundary, with prescribed planar and three-dimensional flagellar waveforms are simulated. Both planar and 'elliptical helicoid' beating cells are predicted to accumulate at distances of approximately 8.5—22 μm from surfaces, for flagellar beating with angular wavenumber of 3π to 4π. Planar beating cells with wavenumber of approximately 2.4π or greater are predicted to accumulate at a finite distance, while cells with wavenumber of approximately 2π or less are predicted to escape from the surface, likely due to the breakdown of the stable swimming configuration. In the stable swimming trajectory the cell has a small angle of inclination away from the surface, no greater than approximately 0.5°. The trapping effect need not depend on specialized non-planar components of the flagellar beat but rather is a consequence of force and torque balance and the physical effect of the image systems in a no-slip plane boundary. The effect is relatively weak, so that a cell initially one body length from the surface and inclined at an angle of 4°–6° towards the surface will not be trapped but will rather be deflected from the surface. Cells performing rolling motility, where the flagellum sweeps out a 'conical envelope', are predicted to align with the surface provided that they approach with sufficiently steep angle. However simulation of cells swimming against a surface in such a configuration is not possible in the present framework. Simulated human sperm cells performing a planar beat with inclination between the beat plane and the plane-of-flattening of the head were not predicted to glide along surfaces, as has been observed in mouse sperm. Instead, cells initially with the head approximately 1.5–3 μm from the surface were predicted to turn away and escape. The simulation model was also used to examine rolling motility due to elliptical helicoid flagellar beating. The head was found to rotate by approximately 240° over one beat cycle and due to the time-varying torques

† Email address for correspondence: D.J.Smith.2@bham.ac.uk

associated with the flagellar beat was found to exhibit 'looping' as has been observed in cells swimming against coverslips.

1. Introduction: the accumulation of motile cells near surfaces

Sperm and other cells that swim with a single flagellum (or 'tail') are known to accumulate 'near' or 'at' surfaces; for example Rothschild (1963) famously observed the 'non uniform distribution of sperm in a drop of bull semen'. Motile sperm are typically observed at high concentrations near the upper and lower inner surfaces of flattened glass capillary tubes and close to the microscope slide or coverslip in wet preparations. In human sperm the effect of gravity has not been observed to have a significant effect, so that the number of cells accumulating on upper and lower surfaces is typically similar (Winet, Bernstein & Head 1984). The phenomenon has long interested researchers, particularly at the interface of mathematical modelling and experimental biology (Winet *et al.* 1984; Lauga *et al.* 2006). However despite a number of studies involving both hydrodynamic modelling and microscopy, the phenomenon has not been fully explained.

Fauci & McDonald (1995) used the immersed boundary technique to simulate sperm accumulation in a two-dimensional flow regime, equivalent to a swimming sheet in three-dimensional flow. Their simulation allowed for fluid/structure interaction between the beating tail and fluid, to show gradual movement of a sperm-like swimmer with a circular head towards an elastic solid interface, as well as phase locking between nearby cells. The underlying physical mechanisms for the accumulation effect however have not yet been explored in detail using this methodology. Lauga *et al.* (2006) modelled *Escherichia coli* as spherical cells with a single helical tail representing the flagellar bundle and were able to give fundamental explanations for both the forces attracting cells to the boundary and the circular swimming paths that cells follow, by analysing the mobility tensors associated with the cell body and tail respectively. The hydrodynamic trapping effect is due to the fact that a cell body moving along and very near an interface will be subject to a torque rotating it towards the surface as it moves forwards. Due to its relatively large size, the effect of the *E. coli* cell body is more significant than any slender body effects on the flagellum. Trapping mechanisms for bacteria are different from mammalian sperm due to fact that the cell body is not nearly as small relative to the flagellum and that bacteria are in the sub-micron scale regime, where electrical effects due to the ionic properties of the surface may be important over distances of the order of 10–100 nm. Further discussion of trapping mechanisms for bacteria is given by Vigeant *et al.* (2002).

Woolley (2003) investigated rodent and ram sperm and described two different surface-trapping effects: (*a*) Cells which roll as they swim exhibit a conical beat envelope, so that when approaching a boundary they enter a configuration in which one edge of the cone is aligned with the surface such that the central axis, and hence thrust vector, points into the surface, as shown in figure 1(*a*). (*b*) Cells which exhibit planar beating near surfaces and are such that the plane of flattening of the sperm head is tilted relative to the beat plane, are subject to a 'hydrofoil' effect as shown in figure 1(*b*). An alternative description of this model is that a lubrication layer exists in the space between the cell body and glass surface and that again the propulsive force of the tail is directed at an angle into the surface. Woolley (2003) has presented experimental evidence for this inclination angle in mouse sperm, and noted that

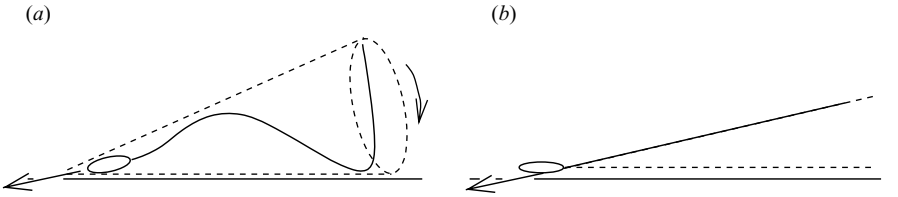

FIGURE 1. The models proposed by Woolley (2003) for boundary accumulation of (*a*) cells that roll as they swim, sweeping out a 'conical envelope', and (*b*) planar beating cells such that the beat plane is inclined to the plane of flattening of the head. Further description is given in the text.

such cells only swim with one particular face against the surface. Surface-trapping effects also occur in the sperm of externally fertilizing species such as sea urchin when examined *in vitro*. Cosson, Huitorel & Gagnon (2003) imaged motile sea urchin sperm cells from *Paracentrotus lividus* and *Arbacia lixula* to show also that an out-of-plane component of the beat appears to result in a directional thrust towards the surface. Their three-dimensional model of the sea urchin beat pattern is essentially a pair of successive helicoids of opposite polarity.

In this study we explore the phenomenon of surface accumulation of cells with the proportions and characteristic beat patterns of human sperm. We investigate the behaviour of both planar and rolling motilities in the vicinity of a surface and simulate the fluid dynamics of the surface accumulation mechanisms proposed by Woolley (2003), applied to human sperm.

2. Fluid dynamical modelling of flagellar cell motility

2.1. *Slender body theory and resistive force theory*

The landmark paper 'Analysis of the swimming of organisms' (Taylor 1951) gave the first mathematical treatment of the propulsion of a flagellum-like object due to travelling bending waves. Taylor advanced one of the two main principles underlying self-propulsion in a purely viscous regime: 'resultant force which the fluid exerts on the body must be zero'. Along with the principle of zero resultant torque later used by Chwang & Wu (1971), these principles are fundamental to all theoretical studies of flagellar motility.

The analysis had certain features which are different from sperm swimming: the organism was represented as a swimming sheet, propagating small-amplitude bending waves along its length. The small-amplitude assumption is not precisely valid for the sperm of most mammalian species but is appropriate for the sperm of the starling (Vernon & Woolley 1999) and has been exploited in studies of the effect of viscoelastic properties (see for example Fulford, Katz & Powell 1998; Lauga 2007, the latter being a substantial direct extension of Taylor's work). Taylor extended his analysis to the three-dimensional flow around a cylindrical body performing planar small amplitude beating, and produced an experimental model sperm which swam by propagating spiral waves (Taylor 1952).

Hancock (1953) coined the term 'Stokeslet' for the singularity solution due to a point force in Stokes flow and used line distributions of Stokeslets and potential dipoles with varying strengths to represent the flow due to the finite-amplitude beating of a flagellum – the basis of slender body theory (SBT) for Stokes flow.

SBT is applicable in any situation where a slender body propels fluid or itself in a very-low-Reynolds-number Newtonian regime and allows cell movement and fluid flow in a three-dimensional domain to be calculated much more efficiently than by solving the Stokes flow equations directly. Hancock was able to show mathematically how a slender body translating tangential to its axis is subject to approximately half of the drag compared with if it translates normal to its axis, a fact which is crucial to zero-Reynolds-number fluid dynamics and the functioning of flagella and cilia. This is referred to as the 'anisotropy ratio' of a slender body. The local approximation to SBT, 'resistive force theory' (RFT) was first developed by Gray & Hancock (1955) and used to analyse sinusoidal planar flagellar beating of sea urchin sperm. They approximated the force on an element of the flagellum as being proportional to the relative velocity of the segment and the fluid, with different 'resistance coefficients' applying to motions normal and tangential to the segment axis. Consideration of this anisotropy ratio allowed elementary mathematical and intuitive arguments for how flagellar wave propagation causes motility. The vast majority of quantitative studies of flagellar fluid dynamics have made use of either SBT or RFT, including the present study.

At the same time as the theoretical analysis, Gray (1955) conducted the first observations of flagellar movement, on sperm of the sea-urchin *Psammechinus miliaris* swimming in sea water. Data had not previously been available due to the fact that the flagellum is too small to visualize using conventional bright-field microscopy, and its movement is too rapid to be discerned clearly by eye. Gray (1955) solved these technical problems by employing dark-field microscopy together with stroboscopic illumination. At frequencies of 30–40 Hz, the flagellum was 'frozen' so that the waveform could be observed. Continous lighting revealed 'flagellar envelope'. This alternated between resembling an ellipse and a straight line, which led Gray to infer that the cell was rolling with a frequency of around 3 Hz and that the flagellar beat envelope was approximately planar.

Despite the internal $9 + 2$ structure of the flagellum being discovered around the same time, it was not agreed whether the flagellum possessed a mechanism for the active production of bending. By analysing the motion of an elastic beam, combined with a simple RFT model of viscous forces, Machin (1958) showed that the emerging waveforms did not resemble those found by Gray (1955) and others. By introducing a simple model of active bending proportional to curvature he was able to produce waveforms that gave a much better qualitative agreement with observations. Later Machin (1963) used a similar analysis to show that nearby flagella will tend to synchronize. Many studies followed, applying RFT to the analysis of forces and bending moments due to observed beating patterns, for example Brokaw (1965, 1970) and Rikmenspoel (1965). RFT has also proved very successful in the modelling of beat pattern production by the interaction of internal mechanics and viscous forces (examples with further references are Hines & Blum 1978; Brokaw 1985).

Gray (1953) noted that in the case of the cell body being small, helical propulsion would likely be ineffective. This was analysed in more detail by Chwang & Wu (1971), who took into account formally the condition of zero net torque and hence were able to model motility due to a rotating helical tail. Genuinely helical waveforms of sperm flagella are likely to be relatively rare, with for example the remarkable images of Woolley & Vernon (2001) being observed for sea urchin sperm in medium with viscosity of approximately 4 Pa s. Nevertheless, sperm of many species roll as they swim which can only occur due to the existence of non-planar components of the flagellar beat.

Pironneau & Katz (1974) used RFT to present insights into optimally energy-efficient beating by examining the small-amplitude case. Extensive work (see for example Brokaw 1972; Hines & Blum 1983; Brokaw 1985) was conducted using RFT to couple internal mechanics and fluid mechanics to understand the emergence of oscillatory propulsive waves. Researchers have continued to use RFT to investigate a number of scientific questions. Examples are (i) Brokaw (2002) in investigating beat pattern emergence in combination with detailed modelling of flagellar internal mechanics, (ii) Kinukawa *et al.* (2005) in finding new interpretations of flagellar beat data and (iii) as reviewed above Lauga *et al.* (2006) on the trapping of bacteria near surfaces.

In the mid-1970s, researchers turned their attention to incorporating boundary effects which are important for mammalian sperm both *in vitro* and *in vivo*. Katz, Blake & Pavieri-Fontana (1975) adapted RFT to modelling slender body motion near and parallel to a surface. They noted that RFT was only strictly valid applied to small-amplitude motions and concluded, '... our understanding of flagellar and ciliary movement and function has reached a level where finite-amplitude theories are needed. We hope that they will be forthcoming'. While Hancock was only able to make limited progress by analytical methods, by the 1970s it was possible to calculate numerical solutions of the SBT integral equation for the force distribution on the flagellum. There are two basic approaches that have been pursued in such numerical calculations: (*a*) applying surface-velocity collocation directly to Hancock's SBT as in Higdon (1979*a*, *b*) or a variant of it as in Smith, Gaffney & Blake (2007) and Clarke *et al.* (2006); (*b*) working with an approximation of Hancock's representation based on 'integrating out' the local Stokeslet/dipole contributions, as first pursued by Lighthill (1976) and later by for example Johnson (1977, 1980), Dresdner, Katz & Berger (1980), Gueron & Liron (1992), Fulford *et al.* (1998) and Gueron & Levit-Gurevich (2001).

Significant work had been carried out on perturbation-theory analysis of slender body motion up to the mid-1970s (reviewed in Smith *et al.* 2007). Shen *et al.* (1975) presented the first study of finite-amplitude swimming of a headless filament, based on the theory of Cox (1970), which expanded the propulsive velocity in terms of the logarithm of the slenderness ratio. This approach allowed significant progress to be made without the requirement for a numerical solution of the SBT integral equation. The work on finite-amplitude swimming that followed appears to have been stimulated by Lighthill's simple and elegant theorem (Lighthill 1976). This result showed that fluid velocity of a point on the flagellar surface near a centreline point $\boldsymbol{\xi}(s_0)$ can be represented as (i) a 'local/Gray–Hancock' contribution $C_N f_N$, due to normal motion of the body and (ii) a 'non-local' contribution given by a line integral of Stokeslets greater than $\delta := a_0\sqrt{\mathrm{e}}/2$ from s_0, where a_0 is the flagellum radius. It was assumed that variations in $\boldsymbol{f}(s)$ are small enough so that $\boldsymbol{f}(s)$ may be taken constant over the interval $s_0 - \delta < s < s_0 + \delta$.

Following this, Dresdner *et al.* (1980) considered a theory which extracted the local Stokeslet/dipole contributions due to both normal and tangential motions, allowing an iterative approach to solving for the unknown force distribution $\boldsymbol{f}(s)$ from an initial estimate obtained from RFT. The cell body was modelled as a sphere, using the well-known representation of a Stokeslet–dipole–rotlet combination. The hydrodynamic interactions of the head and tail, which occur due to the no-slip condition on the head surface, were not taken into account, since in mammalian sperm the head is sufficiently small so that this approximation is relatively accurate, provided that interactions with plane surfaces do not also occur. This approach was used extensively

by Katz and co-workers in the 1980s to investigate the forces, torques and power consumption associated with sperm in a variety of physiological situations (see for example Dresdner & Katz 1981; Baltz, Katz & Cone 1988; Drobnis *et al.* 1988). More recently Fulford *et al.* (1998) used the technique to investigate small-amplitude flagellar propulsion in a linear viscoelastic fluid. A similar approach adapted to Stokes flow in the vicinity of a surface has been very successful for the modelling of waveform emergence in cilia (Gueron & Liron 1992, 1993; Liron 2001) in the form of the Lighthill–Gueron–Liron (LGL) theorem. The efficiency of the technique has proved to be very useful for the modelling of the time-dependent problem of large arrays of interacting cilia, beating due to the interaction of viscous forces and internal mechanics.

A similar approach to SBT was developed by Johnson (1977), later developed to include higher order singularities (Johnson 1980). This was applied in Johnson & Brokaw (1979) to compare the forces calculated by SBT and RFT. This study proved that RFT provides a good estimate for the force distribution for a headless flagellum in the absence of nearby surfaces, even for finite-amplitude motions, provided that *ad hoc* increases are made to both resistance coefficients. The presence of a cell body however meant that a constant correction factor could not be used along the length of the flagellum.

The first application of the direct surface-velocity collocation numerical solution technique directly to SBT appears to be that of Liron & Mochon (1976), as reviewed in detail in Smith *et al.* (2007). The slender body was divided into segments, their size not depending upon the radius or geometry of the body, with the force taken constant on each segment. This discretization led to a matrix equation, with entries comprising Stokeslet integrals, which may be solved directly for the forces. In this early paper the near-field Stokeslet integrals were not computed precisely, instead being estimated from the 'midpoint' value of the Stokeslet on each discretization interval. Higdon (1979*a*,*b*) used accurate, analytically determined Stokeslet and dipole integrals on each segment of the flagellum. An iterative solution approach was employed, but direct solution may be employed equally well. There is a clear analogy between this technique and the boundary integral method for Stokes flow, and indeed Lighthill (1996*b*) explored in detail how the centreline Stokeslet distribution representation can be derived from a surface Stokeslet distribution. Higdon (1979*a*, *b*) modelled finite-amplitude flagellar motions in a way which is both accurate and, as we shall exploit in this study, testable *post hoc*.

All of the above works modelled the cell body or sperm head as a sphere, with combinations of Stokeslets, potential dipoles, rotlets and, in certain cases, the image singularities of Blake (1971) and Oseen (1927; see also Higdon 1979*a*) being used to represent the hydrodynamic effect of the head. The boundary integral method for Stokes flow is a highly versatile technique, allowing the simulation of flows near, or driven by, arbitrary-shaped boundaries such as a non-spherical cell body and a non-planar and non-spherical nearby surface. The technique was first applied by Phan-Thien, Tran-Cong & Ramia (1987) who used a double-layer formulation to model a spheroid cell body propelled by a helical tail. They benchmarked their code against the results of Higdon (1979*b*) and found excellent agreement.

Ramia, Tullock & Phan-Thien (1993) developed the technique further to simulate a three-dimensional helical swimming micro-organism near a circular plate, developing efficient computational methods for solving the time-dependent tracking problem that occurs once the rotational symmetry of the problem is broken by the presence of a boundary. They were able to show that helical swimming cells near a boundary

have a small propulsive advantage but dissipate more power. Their simulation results also replicated the 'circling' of a rolling cell which occurs when swimming near a boundary through the use of their approximate tracking scheme. However they did not address the question of boundary accumulation, and again their beat pattern and cell body proportions were closer to those observed in sea urchin sperm and bacteria than mammalian sperm.

As discussed above, a number of studies have focused on helical swimming micro-organisms. This type of flagellar motility has rarely been reported for spermatozoa, a notable exception being the images of Woolley & Vernon (2001), induced in sea urchin sperm at high viscosity.

Ishijima, Oshio & Mohri (1986) suggested that human sperm cells exhibit 'helicoid' beating, which takes the form of a helix modified by a conical envelope, the cross-section of the cone being flattened from a circle to an ellipse with minor:major axis ratio of 0.2. Either of these forms would provide a rotational component which would explain the rolling observed in motile sperm. It should also be noted that Woolley (1977), investigating the three-dimensional nature of rodent sperm flagella, argued against the possibility of helical or helix-like beating, arguing instead for a 'twisted-planar-type' of beating in these species.

One can show using the torque-balance analysis proposed by Chwang & Wu (1971) that sperm of most mammalian species cannot perform 'true' helical beating, with circular cross-section, at a frequency sufficient to give observed swimming velocities, and indeed this was discussed by Gray: 'The propulsive powers of three-dimensional waves are limited to the extent to which the organism is restrained by external forces from spinning about its own longitudinal axis' (Gray 1953). A difficulty with the pioneering boundary integral study by Phan-Thien *et al.* (1987) was that the cell sizes used to model helically swimming bull sperm had larger volume than those of real cells. The internal control mechanism for the production of planar, helicoid and other forms of beating is an ongoing subject of enquiry (see for example Woolley & Vernon 2001; Brokaw 2002).

2.2. *Computational fluid dynamics and fluid–structure interaction*

In addition to the above studies which used the Newtonian Stokes flow approximation, and which generally prescribe the form of the flagellar beat pattern, there has been growing interest in techniques that allow the modelling of more complex fluid properties such as viscoelasticity; interaction between the fluid, the elastic structure of the flagellum, other nearby structures like boundaries or other cells; and the active mechanism of bending. The waveform hence becomes an emergent property of the coupled 'fluid dynamics–rheology–structure–internal mechanics' model. As reviewed above, Fauci & McDonald (1995) pioneered this approach by applying the immersed boundary method to a two-dimensional model of sperm motility near a boundary and to two nearby sperm. More recent work has involved introducing a discrete viscoelastic structure to the two-dimensional domain (Dillon *et al.* 2007) and combining the immersed-boundary method with the regularized Stokeslet technique (Cortez 2001; Cortez, Fauci & Medovikov 2005) for the modelling of three-dimensional beating.

2.3. *Sperm cell morphology and inter-/intra-species heterogeneity*

Human sperm cells exhibit heterogeneity of length, cell body ('head') size and morphology and motility characteristics. Typical ranges for sperm cell morphology and dimensions are given in Katz *et al.* (1986). In this study we shall take a 'standard' human sperm to have flagellar length 56 μm, including an 11 μm midpiece, flagellar width 0.25 μm and head dimensions $4.5 \times 2.8 \times 1.1$ μm. For the boundary element

representation of the sperm head used in this study, the non-dimensional volume is $0.000037L^3$, where the length scale $L = 56$ μm.

For human sperm, the head volume relative to the flagellar length is approximately 50 times less than that of sperm of the sea urchin. Since the torque on a rotating body scales with the volume – as can be estimated from, for example, the rotlet strength due to a rotating sphere (Higdon 1979*b*) – the torque on a rolling human sperm head will be approximately 50 times smaller than that on a rolling sea urchin sperm head. As discussed above, correctly determining the size of the head and hence the torque for the species under consideration is vital in modelling sperm of a specific species.

3. A hybrid boundary integral/slender body model for sperm motility

3.1. *Fluid mechanics*

The simplest framework for modelling micro-organism motility which takes into account hydrodynamic interaction of the head and flagellum was that used by Higdon (1979*a*, *b*). The flagellum was represented by a line distribution of Stokeslets and potential dipoles, discretized into segments with constant strengths $\boldsymbol{f}_q$ for $q = 1, \ldots, N^t$. The cell body or head was modelled as a sphere, represented by a Stokeslet, a dipole and a rotlet, moving with velocity $\boldsymbol{U}$ and angular velocity $\boldsymbol{\Omega}$. The no-slip condition on the cell body was satisfied by using Oseen's image system for a point force (repeated in Higdon 1979*a*) near a spherical surface. The cell velocity and angular velocity, in addition to the flagellum force distribution, form a set of $N^t + 2$ vector unknowns. Using the no-slip condition, the prescribed motion of the flagellum with respect to the head at N^t collocation points was equated with the body frame fluid velocity field resulting from the unknown force distribution. The conditions of zero total force and torque were also applied, resulting in $N^t + 2$ vector equations. The linear system was then solved iteratively to give the flagellar force distribution and cell translational and angular velocities.

We shall extend this framework to model human sperm which have non-spherical heads and generally accumulate near surfaces. A simple model which (*a*) includes the drag and torque on a non-spherical head near a plane surface, (*b*) includes the hydrodynamic effect of a non-spherical head on the tail and (*c*) satisfies the no-slip condition on the cell body and the plane surface is a boundary-integral representation of the head combined with a slender body representation of the tail. The latter is capable of excellent accuracy and very high efficiency, the tail being represented accurately with just 30–60 vector degrees of freedom for the force per unit length, $\boldsymbol{f}_q$ for $q = 1, \ldots, N^t$. In contrast to the study of Ramia *et al.* (1993) the no-slip boundary is represented using the Stokeslet and image system for Stokes flow in a half-space given in Blake (1971) which we denote as $\boldsymbol{S}^{HS}(\boldsymbol{x}, \boldsymbol{y})$. This will be used in both the boundary integral representation of the head and the slender body representation of the tail.

We shall use a single-layer boundary-integral representation for the head surface ∂H, with traction $\boldsymbol{\phi}(\boldsymbol{X}^h, t)$ for $\boldsymbol{X}^h \in \partial H$. We use a slender body representation for the tail, with force per unit length $\boldsymbol{f}(s, t)$, where $s \in [0, 1]$ is scaled arclength. The velocity field for points in the fluid $\boldsymbol{x}$ outside of, or on, the surface of the sperm is given by

$$\boldsymbol{u}(\boldsymbol{x}, t) = \int\!\!\int_{\partial H} \boldsymbol{S}(\boldsymbol{x}, \boldsymbol{X}^h) \cdot \boldsymbol{\phi}(\boldsymbol{X}^h, t)\, \mathrm{d}\boldsymbol{X}^h + \int_0^1 \boldsymbol{G}(\boldsymbol{x}, \boldsymbol{\xi}(s^*, t)) \cdot \boldsymbol{f}(s^*, t)\, \mathrm{d}s^*. \tag{3.1}$$

The tensor $\boldsymbol{S}$ denotes the appropriate point-force singularity for the domain under consideration, either an infinite fluid or a fluid in the half-space above a plane no-slip boundary $x_3 > 0$. The tensor $\boldsymbol{G}$ denotes a force singularity and potential dipole combination to improve the accuracy of the slender body representation. We discuss the latter in more detail in § 3.4. To implement the single-layer boundary integral we use the Fortran 77 programs given in the section `prtcl_3d` of BEMLIB, the software which accompanies Pozrikidis (2002). The geometry of the body is represented by quadratic triangles; the traction is discretized so that it takes a constant value $\boldsymbol{\phi}_e$ on each element ∂H_e. A 32-element mesh of a sphere is shown in figure 3(*a*), as used in benchmarking results in § 3.5. A deformed spherical mesh, representing a human sperm head with length 4.5 μm, width 2.8 μm and 'thickness' 1.1 μm is shown in figure 3(*b*, *c*). This mesh was produced by modifying an ellipsoid to give the characteristic shape of a human sperm head – with a wide but 'sharp' front edge corresponding to the acrosome. Comparison with a refined 128-element mesh is given in § 3.4, and excellent agreement is found, so the 32-element mesh is used for all simulation results. The slender body representation we use was described in Smith *et al.* (2007), which we briefly review in § 3.2. It involves discretizing the force distribution as being piecewise constant, taking the value $\boldsymbol{f}_q$ for $(q-1)/N < s < q/N$, where $q = 1, \ldots, N^t$.

The point-force Stokeslet singularity for the i-component of the fluid velocity at $\boldsymbol{x}$ resulting from a unit point force acting in the j-direction, located at $\boldsymbol{y}$ is

$$S_{ij}^{\infty}(\boldsymbol{x}, \boldsymbol{y}) = \frac{1}{8\pi\mu}\left(\frac{\delta_{ij}}{r} + \frac{r_i r_j}{r^3}\right), \tag{3.2}$$

where $r_i = x_i - y_i$ and $r^2 = r_1^2 + r_2^2 + r_3^2$; the symbol δ_{ij} denotes the Kronecker tensor. Note that this differs from the definition in Higdon (1979*a*) and Pozrikidis (2002) in the leading factor $1/(8\pi\mu)$. The Stokeslet and image system of Blake (1971) near a no-slip surface $x_3 = 0$ are

$$\begin{aligned} S_{ij}^{HS}(\boldsymbol{x}, \boldsymbol{y}) = \frac{1}{8\pi\mu}\left(\left[\frac{\delta_{ij}}{r} + \frac{r_i r_j}{r^3}\right] - \left[\frac{\delta_{ij}}{R} + \frac{R_i R_j}{R^3}\right]\right. \\ \left. + 2y_3(\delta_{j\alpha}\delta_{\alpha k} - \delta_{j3}\delta_{3k})\frac{\partial}{\partial R_k}\left[\frac{y_3 R_i}{R^3} - \left[\frac{\delta_{i3}}{R} + \frac{R_i R_3}{R^3}\right]\right]\right). \end{aligned} \tag{3.3}$$

The image system is located at $(y_1, y_2, -y_3)$, so that $R_1 = r_1$, $R_2 = r_2$, $R_3 = x_3 + y_3$ and $R^2 = R_1^2 + R_2^2 + R_3^2$. The summation convention is assumed, Latin indices taking values 1, 2, 3 and the index α taking values 1, 2 only. Finally, the infinite-domain potential dipole, also a solution of the Stokes flow equations, is

$$K_{ij}(\boldsymbol{x}, \boldsymbol{y}) = -\frac{1}{4\pi}\frac{\partial}{\partial r_j}\left[\frac{r_i}{r^3}\right] = \frac{1}{4\pi}\left(-\frac{\delta_{ij}}{r^3} + 3\frac{r_i r_j}{r^5}\right). \tag{3.4}$$

We use the infinite-domain potential dipole in all cases, since it is a higher order singularity than the Stokeslet, decaying as $O(1/r^3)$ rather than $O(1/r)$. The error associated with using this in the domain $x_3 > 0$ is therefore negligible, provided that $r_3 \ll y_3$.

As in the work of, for example, Higdon (1979*b*), Dresdner & Katz (1981) and Ramia *et al.* (1993) we shall prescribe the flagellar waveform. Suppressing the s and t dependence, we define $\boldsymbol{\xi}'$ to be the flagellum centreline position in the 'body frame', that is with respect to an origin and axes which translate and rotate with the head. In

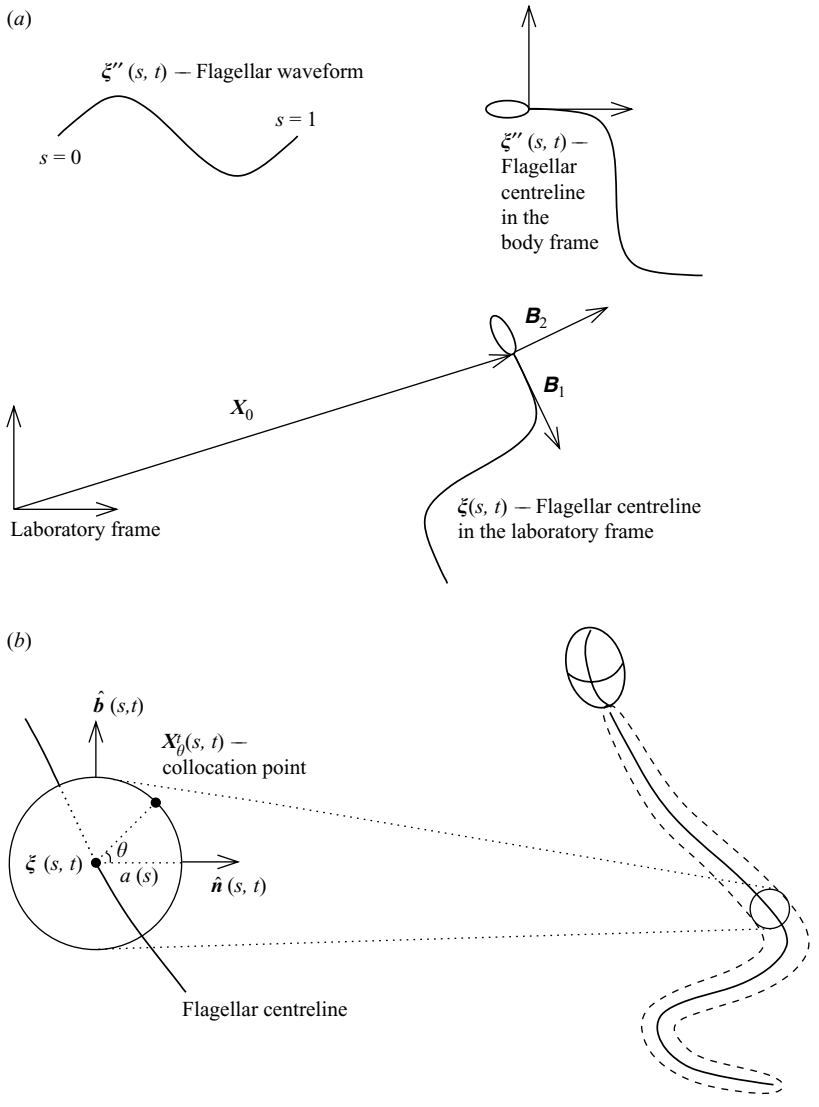

FIGURE 2. (*a*) Schematic showing how specification of the flagellar waveform $\boldsymbol{\xi}''(s,t)$ relates to the body frame flagellar centreline $\boldsymbol{\xi}'(s,t)$ and how this relates to the laboratory frame curve $\boldsymbol{\xi}(s,t)$. (*b*) Schematic showing the 'curved ellipsoid' representation for the flagellum and how collocation points $\boldsymbol{X}^t_\theta(s,t)$ are specified on the circular cross-section about $\boldsymbol{\xi}(s,t)$ by the azimuthal angle θ.

the laboratory frame, the body frame origin, equivalent to the head/tail junction, has coordinate $\boldsymbol{X}_0(t)$, and the body frame axes are given by the matrix $\boldsymbol{B}=[\boldsymbol{B}_1|\boldsymbol{B}_2|\boldsymbol{B}_3]$. This is summarized in figure 2(*a*). As discussed in § A.1, for the Dresdner & Katz (1981) beat pattern we first specify a waveform $\boldsymbol{\xi}''(s,t)$ and then perform translation and rotation to give the body frame centreline $\boldsymbol{\xi}'(s,t)$ satisfying (i) that $\boldsymbol{\xi}'(0,t)$ is at the body frame origin and (ii) that at $s=0$ the flagellum is tangential to the body frame x-axis.

The position of the flagellar centreline in the laboratory frame is given by

$$\boldsymbol{\xi} = \boldsymbol{X}_0 + \boldsymbol{B}\cdot\boldsymbol{\xi}'. \tag{3.5}$$

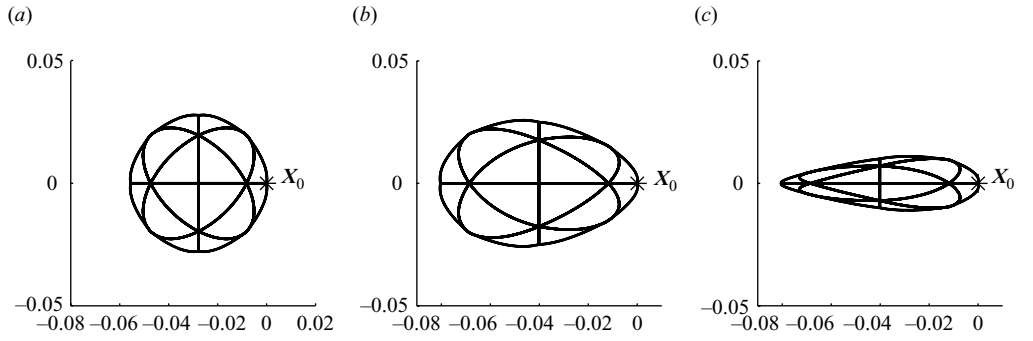

FIGURE 3. (*a*) The 32-element quadratic mesh for the spherical sperm head. This is generated by the BEMLIB routine `trgl_octa` with mesh parameter `ndiv = 1`. The right-hand apex of the head is the location of the head–tail junction $\boldsymbol{X}_0$. (*b*) Top and (*c*) side views of the 32-element quadratic mesh representing a human sperm head. This is generated by deforming a spherical mesh produced by the BEMLIB routine `trgl_octa` with mesh parameter `ndiv = 1`.

The body frame will translate and rotate with *a priori* unknown velocity $\boldsymbol{U}$ and angular velocity $\boldsymbol{\Omega}$. Hence by rigid body mechanics, with respect to the laboratory, the kinematic velocities of points on the head $\boldsymbol{v}_{kin}(\boldsymbol{X}^h)$ and tail $\boldsymbol{v}_{kin}(\boldsymbol{\xi})$ are respectively

$$\begin{aligned} \boldsymbol{v}_{kin}(\boldsymbol{X}^h) &= \boldsymbol{U} + \boldsymbol{\Omega} \wedge (\boldsymbol{X}^h - \boldsymbol{X}_0), \\ \boldsymbol{v}_{kin}(\boldsymbol{\xi}) &= \boldsymbol{U} + \boldsymbol{\Omega} \wedge (\boldsymbol{\xi} - \boldsymbol{X}_0) + \boldsymbol{B} \cdot \dot{\boldsymbol{\xi}}', \end{aligned} \tag{3.6}$$

the final term being the velocity of the flagellum centreline with respect to the body frame, rotated into laboratory coordinates, and the dot in $\dot{\boldsymbol{\xi}}'$ denoting time derivative.

The algorithm calculates the cell velocity $\boldsymbol{U}$, angular velocity $\boldsymbol{\Omega}$, tractions $\boldsymbol{\phi}_e$ and forces per unit length $\boldsymbol{f}_q$, from the specification of the cell position $\boldsymbol{X}_0$, orientation $\boldsymbol{B}$, flagellum position $\boldsymbol{\xi}$ and flagellum velocity $\dot{\boldsymbol{\xi}}$. In the equations that follow we shall equate surface and fluid velocities with respect to the laboratory frame. We impose these conditions at N^h and N^t collocation points on the head and tail respectively and additionally apply force and torque balance over the head and tail.

Applying $\boldsymbol{v}_{kin}(\boldsymbol{X}^h) = \boldsymbol{u}(\boldsymbol{X}^h)$ and $\boldsymbol{v}_{kin}(\boldsymbol{X}^t) = \boldsymbol{u}(\boldsymbol{X}^t)$ to (3.1) we have

$$\begin{aligned} 0 = &\int\!\!\int_{\partial H} \boldsymbol{S}(\boldsymbol{X}^h, \boldsymbol{X}^{h*}) \cdot \boldsymbol{\phi}(\boldsymbol{X}^{h*}, t)\, \mathrm{d}\boldsymbol{X}^{h*} + \int_0^1 \boldsymbol{G}(\boldsymbol{X}^h, \boldsymbol{\xi}(s^*, t)) \cdot \boldsymbol{f}(s^*, t)\, \mathrm{d}s^* \\ &- \boldsymbol{U} - \boldsymbol{\Omega} \wedge (\boldsymbol{X}^h - \boldsymbol{X}_0) \quad \text{for } \boldsymbol{X}^h \in \partial H, \end{aligned} \tag{3.7}$$

$$\begin{aligned} \boldsymbol{B} \cdot \dot{\boldsymbol{\xi}}'(s, t) = &\int\!\!\int_{\partial H} \boldsymbol{S}(\boldsymbol{X}^t_\theta(s, t), \boldsymbol{X}^{h*}) \cdot \boldsymbol{\phi}(\boldsymbol{X}^{h*}, t)\, \mathrm{d}\boldsymbol{X}^{h*} \\ &+ \int_0^1 \boldsymbol{G}(\boldsymbol{X}^t_\theta(s^*, t), \boldsymbol{\xi}(s^*, t)) \cdot \boldsymbol{f}(s^*, t)\, \mathrm{d}s^* \\ &- \boldsymbol{U} - \boldsymbol{\Omega} \wedge (\boldsymbol{\xi}(s, t) - \boldsymbol{X}_0) \quad \text{for } 0 < s < 1. \end{aligned} \tag{3.8}$$

The symbol $\boldsymbol{X}^t_\theta(s, t)$ denotes a point chosen on the surface of the flagellum, which will be displaced by the flagellum radius from the centreline point $\boldsymbol{\xi}(s, t)$, as shown in figure 2(*b*). The choice of the azimuthal angle θ which specifies these points is explained in § 3.2. To close the system, the force balance equation is

$$0 = \int\!\!\int_{\partial H} \phi(\boldsymbol{X}^{h*}, t)\, \mathrm{d}\boldsymbol{X}^{h*} + \int_0^1 \boldsymbol{f}(s^*, t)\, \mathrm{d}s^*, \tag{3.9}$$

and the torque balance, taken with respect to the head–neck junction at $\boldsymbol{X}_0$, is

$$0 = \int\int_{\partial H} (\boldsymbol{X}^{h*} - \boldsymbol{X}_0) \wedge \boldsymbol{\phi}(\boldsymbol{X}^{h*}, t)\, \mathrm{d}\boldsymbol{X}^{h*} + \int_0^1 (\boldsymbol{\xi}(s^*, t) - \boldsymbol{X}_0) \wedge \boldsymbol{f}(s^*, t)\, \mathrm{d}s^*. \quad (3.10)$$

Equations (3.7)–(3.10) are discretized as described above; the boundary integrals are taken as described in Pozrikidis (2002) the slender body integrals are taken using 12 point Gauss–Legendre quadrature for each sub-interval. We then assemble a matrix equation for $3N^h + 3N^t + 6$ scalar variables. The boundary integral over an element ∂H_e evaluated at a collocation point $\boldsymbol{X}^h \in \partial H_e$ will be large but finite. Likewise the integral over a flagellum centreline segment I_q evaluated at a collocation point $\boldsymbol{X}^t_{\theta_q}(s_q, t)$ with $s_q \in I_q$ will also be large but finite, although in this case the point of evaluation is displaced by a finite amount from the singularity location to the flagellum surface.

In zero-Reynolds-number flow, swimming behaviour is directly affected by flagellar kinematics and cell morphology only. Fluid viscosity μ enters the problem only as a multiple of the forces and tractions and without loss of generality is taken to be unity throughout this study – see § 5 for elaboration of the implications of this.

3.2. *Flagellar cross-sectional shape and the slender body collocation method*

In order to form (3.8) we need to choose the surface collocation points $\boldsymbol{X}^t_{\theta_i}(s_q, t)$. We define the vectors $\hat{\boldsymbol{n}}(s, t)$ and $\hat{\boldsymbol{b}}(s, t)$ to be the unit normal and binormal to the flagellum centreline at s. The t dependence is suppressed in this section. For a curved slender body with circular cross-section, the surface of the flagellum is given by $\boldsymbol{X}^t_\theta(s) = \boldsymbol{\xi}(s) + a(s)\hat{\boldsymbol{n}}(s)\cos(\theta) + a(s)\hat{\boldsymbol{b}}(s)\sin(\theta)$ for $0 < s < 1$ and $0 < \theta < 2\pi$, where $a(s)$ is the radius at s.

If the function $a(s)$ takes the constant value a_0, the flagellar surface is a 'curved cylinder', whereas if $a(s) = a_0 s(1 - s)$, then the flagellar surface is a 'curved ellipsoid', as discussed in Smith *et al.* (2007). Slender body theories since the work of Hancock (1953), including those of Higdon (1979*a*) and Dresdner *et al.* (1980), have typically used the 'curved cylinder' representation for the flagellum, which entails the use of the potential-dipole distribution $-(a_0^2/4\mu)K_{jk} f_k^n(s)$, where the normal component of the force density is given by $\boldsymbol{f}^n(s) = [\boldsymbol{f}(s)\cdot\hat{\boldsymbol{n}}(s)]\hat{\boldsymbol{n}}(s)$. This correction reduces the magnitude of the 'azimuthal variation' in the velocity field on $\boldsymbol{\xi}(s_0) + a_0\hat{\boldsymbol{n}}(s_0)\cos(\theta) + a_0\hat{\boldsymbol{b}}(s_0)\sin(\theta)$ for fixed s_0 as the azimuthal angle θ varies from 0 to 2π. A limitation of this representation, as shown in Smith *et al.* (2007), is that the 'end errors' associated with the slender body representation extend along a significant length of the flagellum. The velocity field calculated on the surface of the curved cylinder exhibits spurious variations between collocation points towards the ends of the body. Increasing the number of collocation points does not solve this problem but rather introduces spurious oscillations in the force distribution. Hence with this model, the choice of the azimuthal position of the collocation points has a significant effect on both the calculated force distribution $\mathbf{f}(s)$ and, when simulating cell migration, the trajectory of the cell.

We instead employ the 'curved ellipsoid' representation given in Smith *et al.* (2007), which was based on the work of Chwang & Wu (1975) and Johnson (1980) although implemented differently. This representation reduces the spurious oscillations in the calculated force distribution and the *post hoc* calculated fluid velocity between collocation points. If the slender ellipsoid representing the flagellum has foci at

$s=0$ and $s=1$, with singularities distributed between the foci, then the minor axis is a_0; the major axis is $\sqrt{a_0^2+1/4}$; and the eccentricity $e=1/\sqrt{4a_0^2+1}$. Noting the slightly different definitions of the Stokeslet and potentialdipole, equation (27*a*) of Chwang & Wu (1975) suggests the following form for the slender body singularity distribution:

$$G_{jk}(\boldsymbol{x},\boldsymbol{\xi}(s)) := S_{jk}(\boldsymbol{x},\boldsymbol{\xi}(s)) - \frac{a_0^2}{\mu}s(1-s)K_{jk}(\boldsymbol{x},\boldsymbol{\xi}(s)). \tag{3.11}$$

This differs from the formula used in Smith *et al.* (2007), due to a change in the definition of K_{jk}, and also because the formula used in the previous study was incorrect for the focal length as given – however the difference contributed an error $O(a_0^4)$, which is negligible for the slenderness ratios considered.

The collocation points are then specified by the values θ_q for each $\boldsymbol{X}^t_{\theta_q}(s_q)=\boldsymbol{\xi}(s_q)+a(s_q)\hat{\boldsymbol{n}}(s_q)\cos(\theta_q)+a(s_q)\hat{\boldsymbol{b}}(s_q)\sin(\theta_q)$, where $q=1,\ldots,N^t$, as shown in figure 2(*b*). When performing cell tracking, choosing $\theta_q=0$ for all q, or choosing $\theta_q=\pi$ for all q, introduces a small bias in the left and right directions respectively. Specifying 'alternating' collocation points so that $\theta_{2m}=0$ and $\theta_{2m+1}=\pi$ for $m=1,\ldots,(N^t-1)/2$ greatly reduces bias, producing a value for the cell movement that is intermediate between the results obtained by one-sided collocation.

3.3. *Computational code*

The algorithms were programmed in Fortran 90, and additionally Fortran 77 programs from Pozrikidis (2002) were used. Computations were performed on the University of Birmingham Blue BEAR Opteron cluster, using a single core per simulation. It took approximately 5 hours of wall time to calculate 200 000 time steps, which generally corresponded to 2000 flagellar beat cycles.

To verify the accuracy of the computer code, a number of tests were performed. The force and torque balance algorithm for the slender body was verified by simulating the falling rods problem of Russel *et al.* (1977). While a precise quantitative match to their trajectories was not expected due to the differing implementations of SBT, a qualitative match to the behaviours of 'glancing', 'reversing' and 'colliding' was obtained for the same angles used in their study. The boundary integral code was verified by examining convergence of the far-field velocity due to a translating sphere near a boundary with the stresslet far field given by Blake & Chwang (1974). The force on a unit sphere translating near a surface was compared with the asymptotic theory of O'Neill & Stewartson (1967), giving agreement within 0.18 % for separation $0.1A$ and within 5.4 % for separation of $0.05A$, where A is the sphere radius. In this study we only consider separation distances that are at least 30 % of the head thickness, so the latter error would not occur. Additionally, calculations of the head and tail residuals were made, as described in § 3.6.

3.4. *Cell translation and rotation*

Tracking cell movement entails calculating the position vector $\boldsymbol{X}_0(t_{n+1})$ and orientation matrix $\boldsymbol{B}(t_{n+1})$, from $\boldsymbol{X}_0(t_n)$ and $\boldsymbol{B}(t_n)$ at the previous time step. The boundary integral/slender body algorithm uses $\boldsymbol{X}_0(t_n)$ and $\boldsymbol{B}(t_n)$ together with the flagellar kinematic data at time t_n to calculate the cell velocity $\boldsymbol{U}_n := \boldsymbol{U}(t_n)$ and angular velocity $\boldsymbol{\Omega}_n := \boldsymbol{\Omega}(t_n)$.

We calculate the new values of position and orientation, using a technique based on the Heun second-order algorithm for the numerical solution of ordinary differential

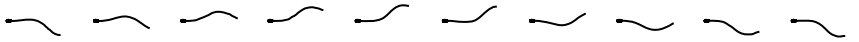

FIGURE 4. The beat cycle data of Dresdner & Katz (1981) with wavenumber $k = 2\pi$, divided into 10 intervals, shown in the body frame. The frames are separated in the x direction for clarity; this does not represent the motion of the sperm.

equations:

$$\left.\begin{array}{l}\text{time step } n, \text{ position } \boldsymbol{X}_0(t_n), \text{ axes } \boldsymbol{B}(t_n);\\ \quad \text{calculate velocity } \boldsymbol{U}_n \text{ and angular velocity } \boldsymbol{\Omega}_n \text{ from data at t} = t_n;\\ \quad \text{set } \boldsymbol{X}_0^* = \boldsymbol{X}_0(t_n) + (\delta t)\boldsymbol{U}_n;\\ \quad \text{set } \boldsymbol{B}^* = \boldsymbol{R}[(\delta t)\boldsymbol{\Omega}_n] \cdot \boldsymbol{B}(t_n);\\ \quad \text{calculate } \boldsymbol{U}_{n+1}, \boldsymbol{\Omega}_{n+1} \text{ from } \boldsymbol{X}_0^*, \boldsymbol{B}^* \text{ and beat data at t} = t_{n+1};\\ \quad \text{set } \boldsymbol{X}_0(t_{n+1}) = \boldsymbol{X}_0 + (\delta t/2)(\boldsymbol{U}_n + \boldsymbol{U}_{n+1});\\ \quad \text{set } \boldsymbol{B}(t_{n+1}) = \boldsymbol{R}[(\delta t/2)(\boldsymbol{\Omega}_n + \boldsymbol{\Omega}_{n+1})] \cdot \boldsymbol{B}(t_n);\\ \text{go to time step } n+1.\end{array}\right\} \quad (3.12)$$

To test this algorithm, we simulated swimming over a single beat cycle with 100 and 400 time steps per beat. We found that the cell translation distance agreed to within 0.08 %, confirming that the temporal discretization is not a significant source of error.

We used the same test for the spatial discretization of the 'human' sperm head. Comparing discretizations of 32 and 128 elements, achieved with the parameters `ndiv = 1` and `ndiv = 2`, we found that in the infinite domain the cell translation result agreed within 0.04 % and initially $0.2L$ above a no-slip surface within 0.0025 %, confirming that the spatial discretization used is not a significant source of error.

3.5. *Swimming in an infinite domain: comparison with the results of Dresdner & Katz (1981)*

We first present results for comparison with those of Dresdner & Katz (1981), for their 'activated human sperm' beating model, as depicted in figure 4 and described in § A.2. Their results were calculated using the model given in Dresdner *et al.* (1980), which used the Hancock (1953) SBT, modified to be more efficient using the theorem of Lighthill (1975). The essence of Lighthill's theorem is that near-field singularity contributions are integrated to give an RFT-type term, while far-field potential-dipole terms are neglected, leaving only far-field Stokeslet integrals. The collocation issues discussed above are circumvented by evaluating the fluid velocity on the centreline rather than the flagellum surface.

In this study we shall not make these simplifications but rather solve the problem using surface-velocity collocation directly. For comparison with the results of Dresdner & Katz (1981), in this section we use the tail length scale of 45 μm, the beat frequency 14 Hz and a spherical head of radius 1.25 μm with the fluid assumed to be infinite. The flagellum was represented by $N^t = 60$ degrees of freedom.

We find that using the 'curved ellipsoid' representation for the tail, with maximum radius $(0.25/45)L$, over one beat period, the point $\boldsymbol{X}_0$ translates from $(0, 0, 0)$ to $(-0.0564L, 0.0297L, 0.0000L)$. The cell positions at the beginning, middle and end of a beat cycle are shown in figure 5. The calculated cell velocity is therefore 40.2 μm s^{-1}. This compares with the larger value of 43 μm s^{-1} given by Dresdner & Katz (1981). The calculated velocity for our model is not heavily dependent on the choice of collocation points.

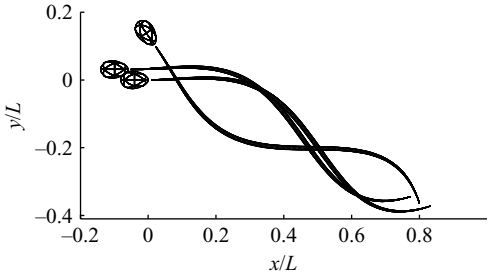

FIGURE 5. Sperm locations and flagellum shapes at the beginning, middle and end of one beat cycle. The cell 'yaws' to one side and then returns having progressed forward slightly. The simulation was performed with the 'activated' beating model of Dresdner & Katz (1981) and the 'human' sperm head mesh.

For the cylindrical representation, varying the position of the collocation points from $\theta_q = 0$ to $\theta_q = \pi$ for all q results in a change in the prediction of swimming speed of 19 %. With a Stokeslet-only representation, the variation being 67 % is even more unacceptably large. For the ellipsoidal representation, the change in prediction of swimming speed with change in choice of collocation points is 1.4 %, showing that the ellipsoidal representation with associated dipole singularities is preferable for robust cell tracking with the surface-velocity collocation approach. The main differences between our present approach and the work of Dresdner & Katz (1981) are (*a*) that the no-slip condition is now satisfied accurately on the sperm head and (*b*) that the tail forces are calculated directly by surface-velocity collocation, rather than by the iterative scheme described in Dresdner *et al.* (1980), allowing for greater refinement in the discretization of the force distribution. In the remainder of the paper we make the additional refinement of considering a physiologically shaped sperm head.

3.6. *Numerical residuals*

To verify *a posteriori* the accuracy of each time step, we calculate the fluid velocity at points on the surface of the head and flagellum and compare them to, respectively, $\boldsymbol{U} + \boldsymbol{\Omega} \wedge (\boldsymbol{X}^h - \boldsymbol{X}_0)$ and $\boldsymbol{U} + \boldsymbol{\Omega} \wedge (\boldsymbol{X}^t - \boldsymbol{X}_0) + \dot{\boldsymbol{\xi}}$, as discussed in Smith *et al.* (2007). To quantify the accuracy on the head, we employ a scaled residual measure on each element e, denoted r_e. The residual is given by the difference between the 'kinematic boundary velocity' $\boldsymbol{v}_{kin}(\boldsymbol{X}^h) = \boldsymbol{U} + \boldsymbol{\Omega} \wedge (\boldsymbol{X}^h - \boldsymbol{X}_0)$ of the point $\boldsymbol{X}^h$ and the fluid velocity calculated from (3.1) with $\boldsymbol{x} = \boldsymbol{X}^h$. The element residual function is then scaled with respect to the maximum surface velocity on the element:

$$r_e(\boldsymbol{X}^h) = \frac{|\boldsymbol{v}_{kin}(\boldsymbol{X}^h) - \boldsymbol{u}(\boldsymbol{X}^h)|}{\max_{\boldsymbol{x} \in \partial H_e} |\boldsymbol{v}_{kin}(\boldsymbol{x})|}. \tag{3.13}$$

The element is parametrized as in Pozrikidis (2002) as $0 < \xi < 1$ and $0 < \eta < \xi$. In what follows we use (x, y, z) coordinates instead of index notation (x_1, x_2, x_3), and the plane surface will be at $z = 0$. Figure 6 shows the residual on various representative elements of the head mesh, for example, near the head/flagellum junction $\boldsymbol{X}_0$ and at the front of the cell where the highest curvatures occur. Additionally, figure 6(*f*) shows the residual on element 21, which is one of the 4 elements adjacent to the no-slip boundary. The scaled residual on element 21 is less than 3 % for $Z_0 \geqslant 0.020L$, but for $Z_0 = 0.015L$ the error reaches 6 %.

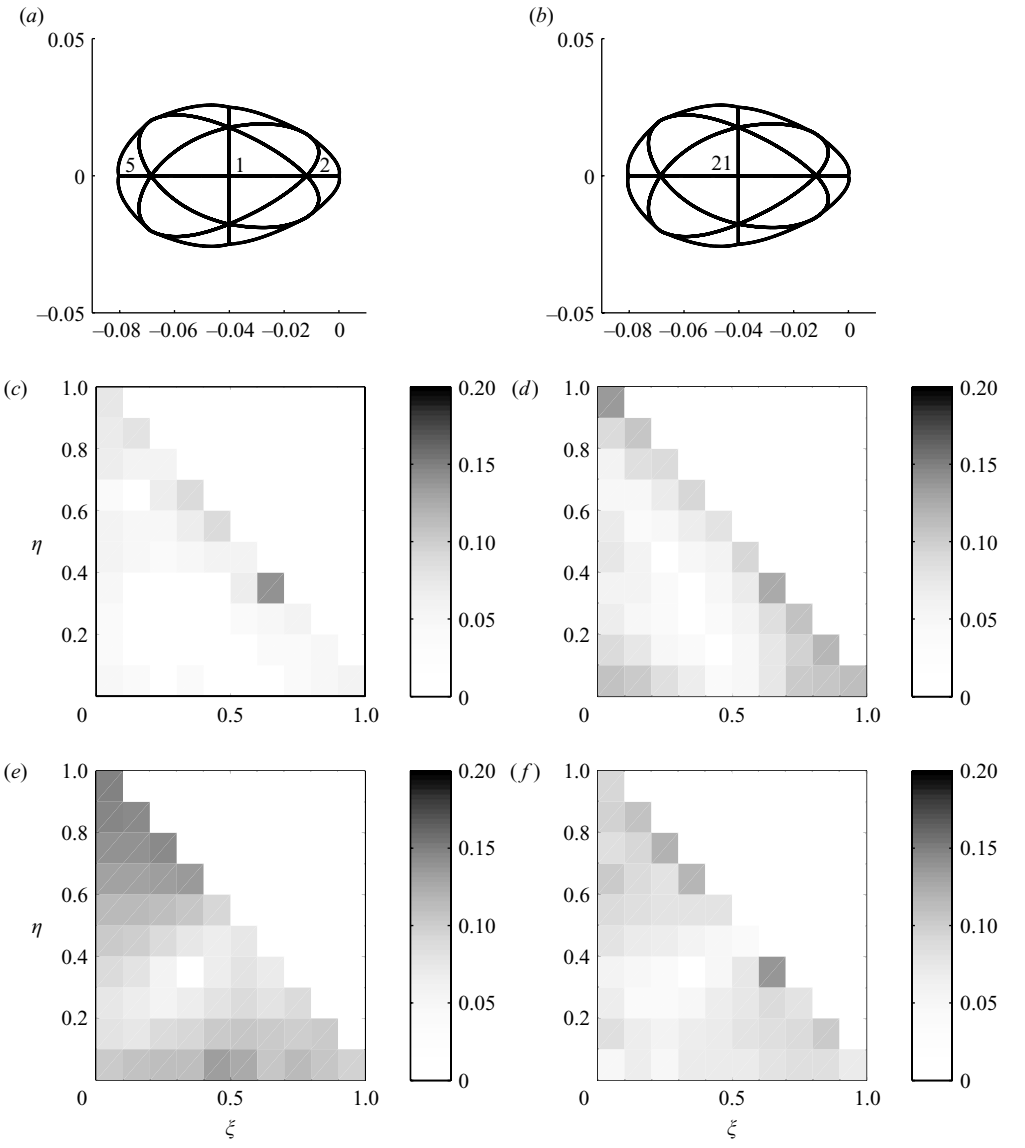

FIGURE 6. (*a*) Top view and (*b*) bottom view of the 32-element 'human' sperm head mesh, showing the elements 1, 2, 5 and 21 used for residual testing. (*c*)–(*f*) The fluid velocity residual on various elements, scaled with respect to the maximum velocity on the element, as defined in (3.13). (*c*) The residual in the infinite domain on element 1. (*d*) The residual in the infinite domain on element 2, one of the four elements adjacent to the head/neck junction. (*e*) The residual in the infinite domain on element 5, one of the elements with the highest curvature. (*f*) The residual when the mesh is close to a no-slip boundary, on element 21, which is one of the elements adjacent to the boundary, where height $Z_0 = 0.025$.

Figure 7 shows the calculated u_1, u_2 and u_3 fluid velocity components on points along the surface of the flagellum, alongside the 'kinematic boundary condition' components of $\boldsymbol{v}_{kin}$ calculated from the flagellar movement and cell velocity and translation. The fluid velocity varies smoothly between collocation points, except for at the tip of the flagellum, beyond the final collocation point, over 1/120th

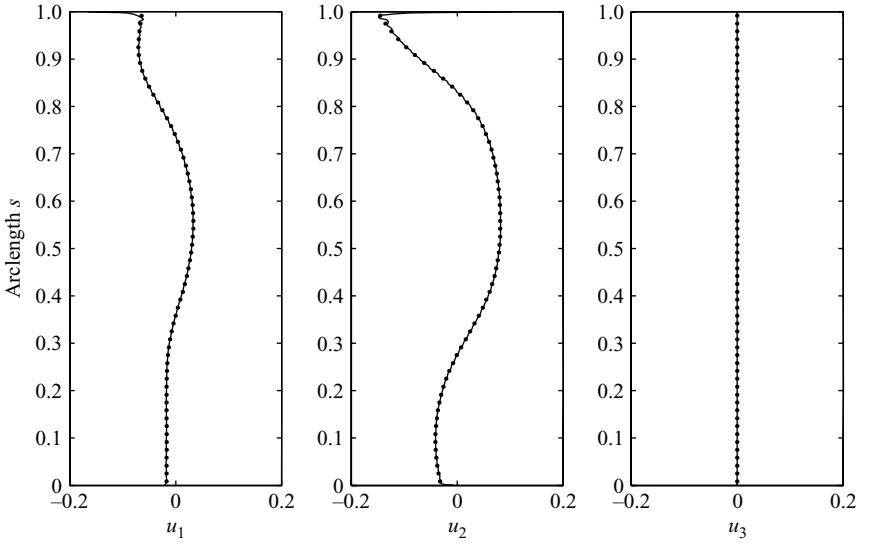

FIGURE 7. Accuracy testing for the flagellum: comparison of the computed flagellar surface fluid velocity components $\boldsymbol{u}(\boldsymbol{X}^t_{\theta=0}(s))$ and the 'kinematic boundary condition' surface velocity components of $\boldsymbol{v}_{kin}$ for the Dresdner & Katz (1981) flagellar beat and the 32-element 'human' head mesh. The tail was discretized with 60 constant-force intervals, and infinite domain singularities were used.

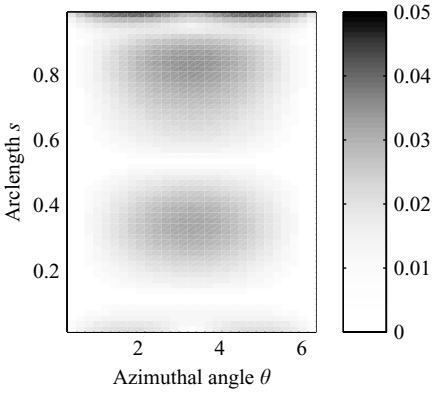

FIGURE 8. Accuracy testing for the flagellum: the azimuthal variation with θ in the magnitude of the computed flagellar surface fluid velocity $|\boldsymbol{u}(\boldsymbol{X}^t_\theta(s))|$, scaled with respect to the maximum velocity of any point on the flagellum; infinite domain singularities were used.

of the length of the flagellum. This very localized end error does not result in high sensitivity of the calculated force distribution to variations in the choice of collocation points except at the tip of the flagellum. This compares favourably with the 'cylinder' representation, as shown in Smith *et al.* (2007). Figure 8 shows $|\boldsymbol{u}(\boldsymbol{X}^t_\theta(s)) - \boldsymbol{u}(\boldsymbol{X}^t_{\theta=0}(s))|$, scaled with respect to the maximum value of the speed along the flagellum – the magnitude of the azimuthal variation of the flagellum surface velocity field.

4. Simulation study results

In the following sections, we use the hybrid boundary integral/slender body model to investigate aspects of cell migration: the effect of head geometry and a nearby no-slip boundary on cell progression, the surface accumulation phenomenon for planar beating cells and finally the surface accumulation phenomenon for three-dimensional beating cells.

4.1. *The effect of head geometry and surface proximity on cell progression*

It may be speculated that the flattened shape of the human sperm head allows for more rapid progression through liquid. We simulated progression of cells over one beat cycle, which have the same volume but are either spherical or 'physiological' shape. The physiological head allows more rapid movement for a given beat pattern, by a factor of 2.8 %. The spatial convergence test for the head mesh discussed in § 3.4 demonstrates that this difference is not a numerical artefact. Analysing the resistance matrix using the BEMLIB routine `prtcl3d` shows that the resistance to forward motion of the physiological head is actually 2 % more than the spherical head, due to the fact that its surface area is 30 % greater. The resistance to rotation of the physiological head about the body frame z-axis is more than doubled compared with the spherical head, which has the effect of decreasing yawing of the head, resulting in increased overall forward progression.

The proximity of the no-slip surface has a negligible effect of less than 0.003 % on progression at a distance of $2.0L$, but at a distance of $0.2L$, equivalent to approximately 12 μm, the boundary results in approximately a 3.6 % increase in swimming velocity compared with swimming in an infinite fluid for the 'human' mesh. Very similar results are observed with the ellipsoid representation for differing choices of collocation points.

4.2. *'Finite distance' surface accumulation of a planar beating cell*

The simulation model was used to simulate swimming of a cell initially parallel to, and at height $Z_0 = 1.0L$ above, the plane boundary $z = 0$. The beat pattern used was again that given by Dresdner & Katz (1981), with a range of values for the wavenumber k. Figure 9 shows the trajectories of cells with $k = 2\pi$, 3π and 4π. For $k = 2\pi$, the parameter used by Dresdner & Katz (1981) to simulate 'activated human sperm' swimming in semen, the cell turns away from the surface and escapes. For $k = 3\pi$ and $k = 4\pi$, the cell behaves differently: it turns towards the surface and then away, performing a series of oscillations which converge to a stable swimming height above the surface. Convergence happens more quickly for $k = 4\pi$, with the stable swimming height being reached in approximately 80 body lengths.

Figure 10(*a*) shows the effect of wavenumbers from $k = \pi$ to $k = 4\pi$ on surface accumulation behaviour. For $k \leqslant 2\pi$, the cell is predicted to escape. For $k = 2.1\pi$, 2.2π, simulation results are inconclusive: over a period of 400 000 time steps the cell exhibits oscillations which grow in size. It appears likely that the cell would escape, but it is not possible to demonstrate this conclusively. For $k = 2.3\pi$, 2.4π the cell exhibits converging oscillations, but a converged trajectory and hence stable value of Z_0 was not obtained in the simulation period of 400 000 time steps. For $k \geqslant 2.5\pi$ the cell is predicted to converge to a constant height Z_0 that falls as k is increased. For a cell with $k = 3\pi$ the accumulation height would be $Z_0 = 0.31L$, corresponding to approximately 17 μm for a human sperm cell. In the stable trajectory, the cell is found to be slightly tilted away from the surface. Figure 10(*b*) shows the effect of wavenumber on this angle. Cells with the smallest values of wavenumber for which accumulation occurs

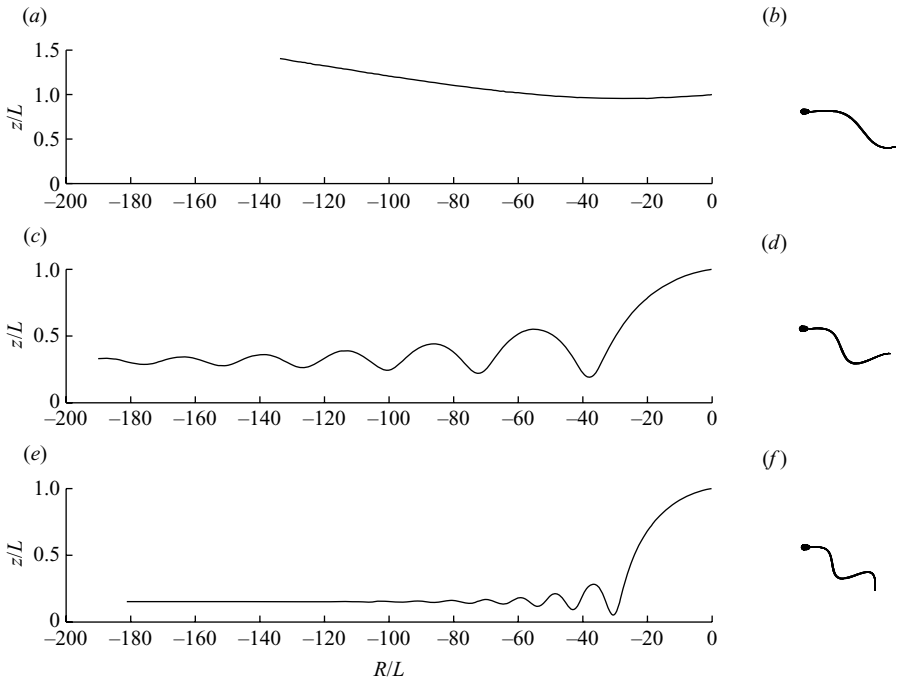

FIGURE 9. Simulation results for planar beating cells with wavenumbers $k = 2\pi$, 3π, 4π, initially swimming parallel to a plane boundary, starting from $z = 1.0L$. (*a*),(*c*),(*e*) The trajectory of $\boldsymbol{X}_0$, using the coordinates $R = -\sqrt{x^2 + y^2}$ and z, with $z = 0$ corresponding to the no-slip boundary. Results for simulations consisting of 200 000 time steps of duration 1/100th of a beat period. With a typical frequency value of 14 Hz this corresponds to total time duration of approximately 140 s, the time step being 0.00071 s. (*b*),(*d*),(*f*) A top view of the flagellar waveform, showing the variation due to wavenumber. (*a*) For $k = 2\pi$, after initially moving slightly towards the boundary, the cell ecapes. (*c*) For $k = 3\pi$, the cell performs a series of oscillations towards and away from the boundary, with decreasing amplitude, giving eventual convergence to a flat trajectory. (*e*) For $k = 4\pi$, a similar effect occurs, only the convergence is more rapid, and the eventual separation is smaller.

exhibit the smallest inclination angles. Extrapolating from the values given in the figure suggests that a wavenumber between 2.3π and 2.4π corresponds to an angle of 0° – suggesting that these are indeed the minimal wavenumbers for which this phenomenon may occur with the prescribed beat pattern.

4.3. *'Elliptical helicoid' flagellar beating and surface accumulation*

As discussed in § A.3, it has been inferred from experimental observations that both human and bull sperm typically execute an 'elliptical helicoid' flagellar beat. A simple parameterized model of this type of beating is given in (A5) – a left-handed helix, modified so that it has (i) linearly increasing amplitude starting from the head–tail junction and (ii) elliptical cross-section with minor:major axis ratio of $\alpha_3 : \alpha_2$, which we choose to be 1 : 5 based on the observations of Ishijima *et al.* (1992). Top, side and front projections of this beat pattern are shown in figure 11(*a–c*); a montage of swimming cell positions is given in figure 11(*d*) for initial height $Z_0 = 1.0L$ with the sperm initially parallel to the surface.

The non-planar component of the flagellar beat results in rolling of the cell as it swims due to torque balance. With the wavenumber $k = 3\pi$ we again predict gradual

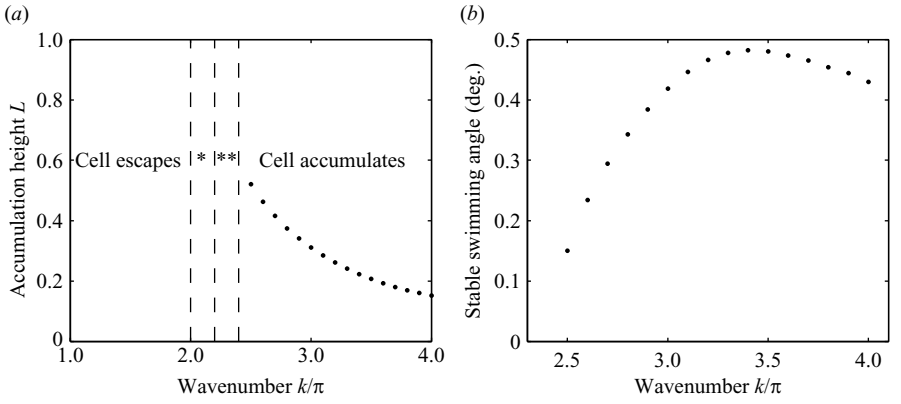

FIGURE 10. Surface accumulation for planar beating cells with varying wavenumber. (*a*) Summary of the effect of wavenumber, expressed as a multiple of π, on accumulation behaviour and eventual stable accumulation height, for a cell initially at $z = 1.0L$ and parallel to the surface. For $k \leqslant 2\pi$ the cell escapes from the surface. (*) For $k = 2.1\pi, 2.2\pi$, cells simulated for 400 000 time steps exhibit turns towards and away from the surface; however the oscillations are of growing amplitude. (**) For $k = 2.3\pi, 2.4\pi$, cells simulated for 400 000 time steps exhibit oscillations of decreasing amplitude, suggesting that an eventual stable height will be reached. For $k \geqslant 2.5\pi$, cells are found to converge to a stable height above the surface. (*b*) The effect of wavenumber, expressed as a multiple of π, on the stable inclination angle away from the surface.

convergence of the swimming path over 2000 beat cycles, although the convergence is not as rapid as the beat pattern used to produce figure 9. We also tested cells with $k = 2\pi$ and $k = 4\pi$ and obtained similar results to the planar case – respectively escape and accumulation (results not shown). Setting $\alpha_3 = 0$ so that the beat pattern is planar, the surface accumulation behaviour still occurs. Swimming is not as rapid in the rolling case, since rolling of the cell reduces the apparent wave speed in the laboratory frame – as discussed by Gray (1953) and Chwang & Wu (1971).

4.4. *'Elliptical helicoid' beating and head movement*

The present modelling framework allows the prediction of cell rolling behaviour resulting from specifications of the flagellar beat, taking into account the important effect of the head geometry, which influences the force and torque balance on the cell. Figure 12 shows (*a*) a montage of cell positions at every half beat cycle and (*b*) the head positions at the beginning, middle and end of a beat cycle. Viewed from the front, the head rolls clockwise to counterbalance the torque exerted by the anticlockwise-rotating flagellum. The head rolls in synchrony with the plane of flattening of the flagellar beat due to the way the flagellar beat is specified, consistent with the observations of Ishijima *et al.* (1992) and the fact that the flagellum does not rotate with respect to the head in eukaryotic cells, in contrast to bacteria. The trajectory of the point $\boldsymbol{X}_0$ is shown in figure 12(*c*). This shows that the rate of rolling of the cell is not constant, as was the case for a cell with a pure helical beat as considered by Higdon (1979*b*). The non-constant rolling rate occurs because the non-planar component of the beat that generates the roll grows in amplitude as it propagates along the tail. The result is two 'loops' per beat cycle, and this simple model of three-dimensional movement produces qualitative similarities with the observations of Woolley (2003) of the 'flagelloid curve' trajectory of a cell swimming against a coverslip, as shown in figure 12(*d*, *e*).

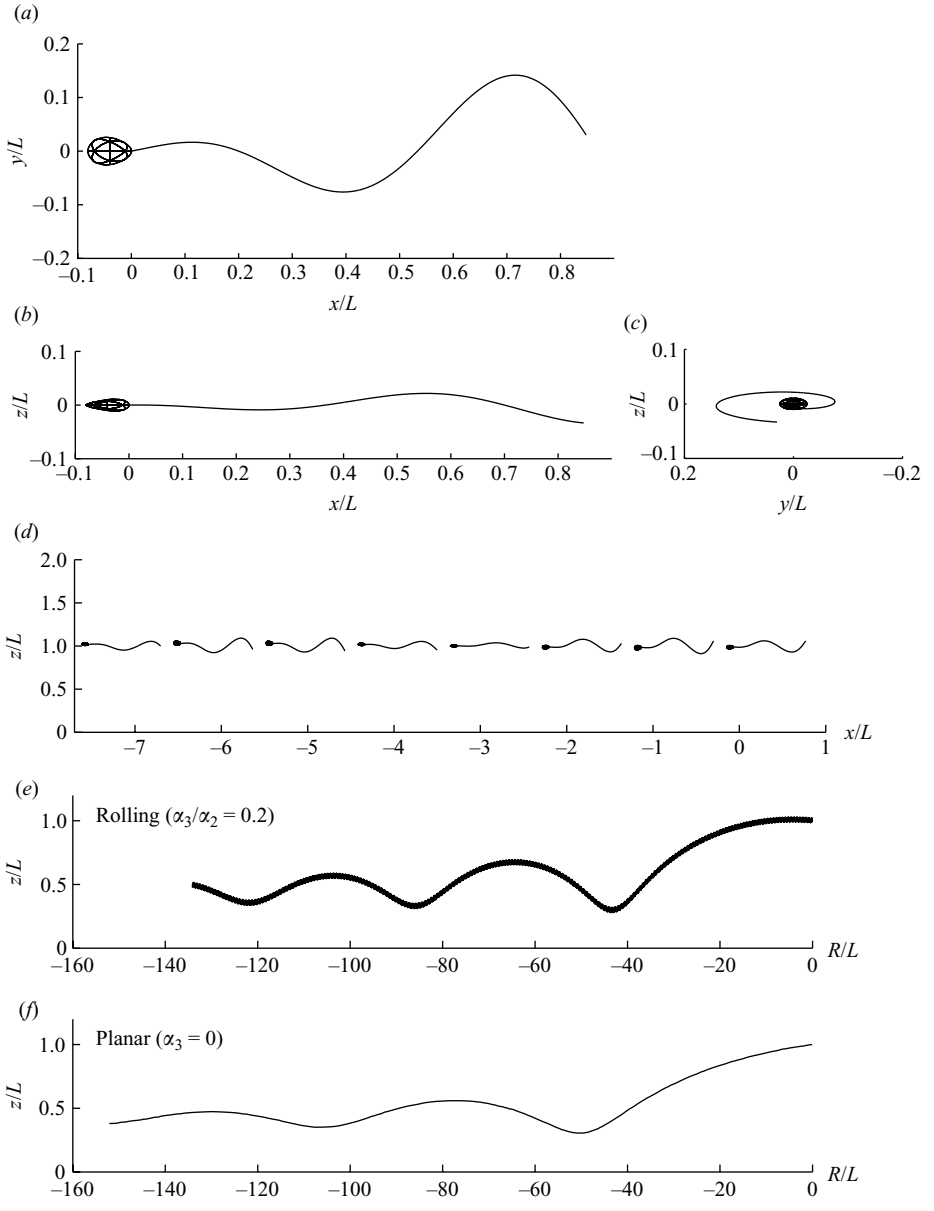

FIGURE 11. 'Elliptical helicoid' flagellar beat pattern, with amplitude parameter $\alpha_2 = 0.2$, minor:major axis ratio $\alpha_3/\alpha_2 = 0.2$ and wavenumber $k = 3\pi$. The resulting surface accumulation behaviour is also presented. (*a–c*) Top, side and front views of the flagellar waveform. (*d*) Rolling motility due to the three-dimensional flagellar beat, viewed from the side with the no-slip surface coinciding with the x-axis. (*e*) Long time scale trajectory of $\boldsymbol{X}_0$ for elliptical helicoid swimming, plotted using the coordinates $R = -\sqrt{x^2 + y^2}$ and z. (*f*) Long time scale trajectory for the corresponding planar beat pattern, equivalent to setting the aspect ratio to be zero. Simulations were run for 2000 beat cycles, with time step 1/100th of a beat period, starting parallel to the surface and at height $z = 1.0L$.

4.5. *The effect of initial angle of inclination*

Cells approach surfaces with an angle of inclination, and so we investigated the effect of this on whether the cell will be trapped. For this we used the rolling motility

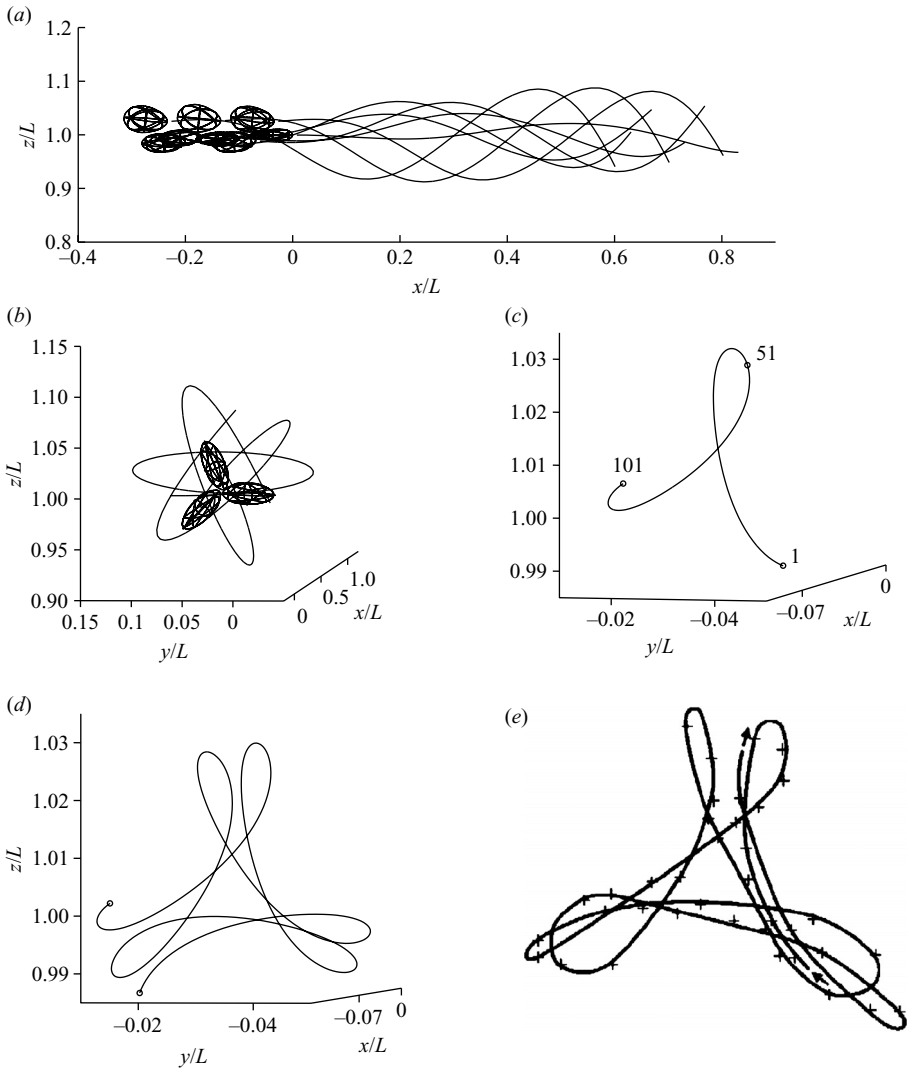

FIGURE 12. Cell rolling due to the elliptical helicoid beat pattern with aspect ratio $\alpha_3/\alpha_2 = 0.2$, amplitude $\alpha_2 = 0.2$ and wavenumber $k = 3\pi$. (*a*) Montage showing the cell position at every half-beat cycle or every 50th time step. (*b*) Montage showing head rolling at time steps 1, 51 and 101, corresponding to one complete beat cycle. The helical tail beats in an anticlockwise direction viewed from the front. By torque balance, the whole cell must rotate clockwise to balance this. The head rolls clockwise approximately 240° in one beat cycle with the chosen parameters. (*c*) This rolling is evident in the $\boldsymbol{X}_0$ trajectory plot, which shows a continuous clockwise rotation of the cell, with a 'looping' behaviour caused by a higher rotation rate at the middle and end of the beat cycle. (*d*) The looping behaviour over three beat cycles, which shows remarkable qualitative similarity with (*e*) the looping behaviour of sperm observed by Woolley (2003) swimming into a coverslip. D. M. Woolley (Reproduction 126, 264) copyright the Society for Reproduction and Fertility 2003, Reproduced by Permission.

pattern described in the previous sections. Results are shown in figure 13. For angles of 0°–2° (figure 13*a*), the cell performs the oscillatory converging trajectory. For angles of 4°–6°, the cell 'rebounds' from the surface and escapes (figure 13*b*, *d*). For angles of 8° or greater, the cell is predicted to collide with the surface, before which point the current modelling framework is no longer valid (figure 13*c*, *e*).

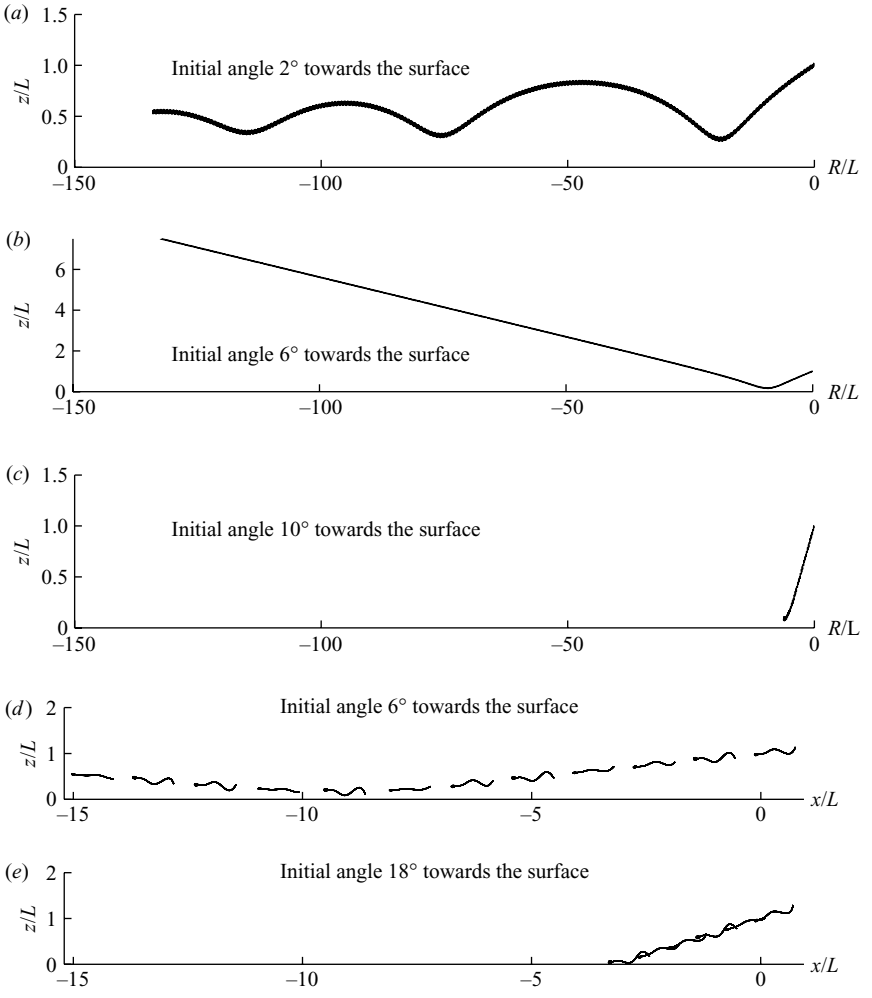

FIGURE 13. Simulation results for the elliptical helicoid beat pattern with different initial angles of inclination towards the surface, for a cell with parameters $\alpha_2 = 0.2$, $\alpha_3/\alpha_2 = 0.2$ and $k = 3\pi$. For initial angles of 0°to 2°, the cell converges to a constant height. For angles of 4° to 6°, the cell 'rebounds' from the surface and escapes. For angles of 8°to 20°, the simulation halts because either the flagellum or the head collides with the surface. Example results are given for (*a*) 2°, (*b*) 6° (note the differing z scale) and (*c*) 10°. (*d*) Montage of cell positions with initial angle of attack 6°. The cell approaches the surface closely and then escapes. (*e*) Montage of cell positions with initial angle of attack 18°. The cell aligns with the surface in the manner suggested by Woolley (2003); however further simulation of this phenomenon is not possible within the current framework.

We also carried out simulations for a planar beating cell with $k = 3\pi$ and an initial angle of inclination to the surface (results not shown). The simulations also predicted accumulation for initial angle of 2° and escape for initial angle of 4°.

4.6. *Simulations of cells swimming 'against' a surface*

Figure 1 shows two possible models by which cells can swim 'against' surfaces. The first holds that cells sweeping out a conical envelope, such as those swimming with the elliptical helicoid beat pattern, may align so that one side of the cone is against the surface, resulting in the propulsive force of the flagellum being directed into the

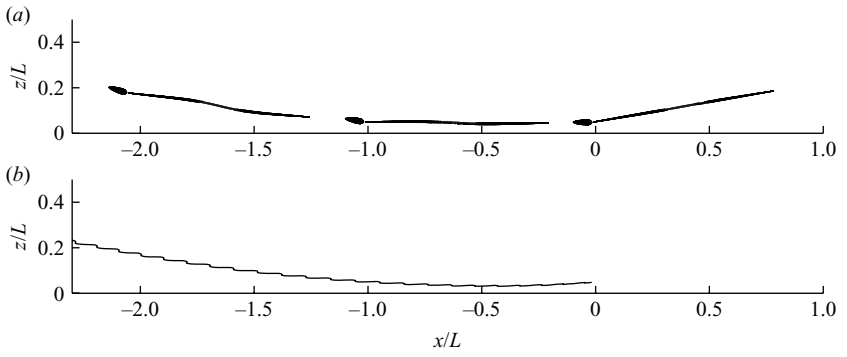

FIGURE 14. Simulating the 'hydrofoil' model of Woolley (2003) for a planar beating cell with the proportions of a human sperm and wavenumber $k = 3\pi$: example results with angle of inclination between the head and the beat plane of 10° and initial height $z = 0.05L$. Simulations were performed with 400 time steps per beat cycle; the cell is viewed from the side so that the beat plane is not visible. The cell 'lifts' off the surface. (*a*) Montage of cell positions at time steps 1, 1001 and 2001. (*b*) Trajectory of $\boldsymbol{X}_0$ over the first 9120 time steps.

surface. While the current modelling framework does not allow the simulation of either the head or flagellum being in very close proximity to $z = 0$, it is possible to test whether the initial stage of such a trajectory may occur. Figure 13(*e*) shows the alignment of such a cell against a surface for initial angle of inclination of 18°.

The second model, based on observations of mouse sperm, holds that if there is a small angle of inclination between the beat plane and the plane of flattening of the head, a cell may 'glide' along a surface, with the propulsive force of the flagellum pushing the head towards the surface. This could result in the cell moving forward while remaining a very small distance from $z = 0$. We tested whether this model could apply to human sperm, by combining the human sperm head mesh with the Dresdner & Katz (1981) planar beat, with $k = 3\pi$. Example results are shown in figure 14 for an inclination angle of 10° and initial height $Z_0 = 0.05L$. The cell quickly lifts off the surface and escapes. We tested angles of up to 12° and found that the same phenomenon occurs. Even for initial angle of inclination of 0°, a cell starting at this height is still deflected away sufficiently to escape. We repeated the simulations for Z_0 initially $0.03L$ and obtained similar results. Simulating a cell initially closer to the surface is not possible within the current framework.

5. Discussion

We studied the fluid mechanics of human sperm swimming in a Newtonian viscous fluid near a no-slip planar boundary, in order to explain and interpret the observations of Rothschild (1963), Winet *et al.* (1984) and Woolley (2003). We formulated a hybrid boundary integral/slender body model of a human sperm, with physiological head size and proportions. We investigated four possible beat patterns: the planar 'activated human' model proposed by Dresdner & Katz (1981), a simple model of an 'elliptical helicoid' flagellar beat, the corresponding planar degenerate case and finally the 'activated human' beat pattern combined with a tilt angle between head and beat plane.

Our simulation results predict that a planar beating model of human sperm cell initially one body length away from and oriented parallel to a surface, with sufficiently large wavenumber, is 'steered' by the surface to an equilibrium trajectory, resulting in surface accumulation. The simulations suggest that the critical value of

the wavenumber is approximately 2.2π, although simulation results were inconclusive in the range 2.0π–2.4π. The cell initially performs an oscillatory motion with decaying amplitude, which continues with the cell converging on an equilibrium height at which it swims in a stable manner a small angle of inclination away from the surface. The oscillations occur over relatively long distances, typically tens of body lengths, and as such would occur over observation periods of tens of seconds. For a cell with wavenumber $k = 3\pi$ we predict that the equilibrium height is approximately 17 μm. The equilibrium height is reduced as the wavenumber is increased, so that a cell swimming with a wavenumber of $k = 4\pi$ is predicted to swim at approximately 8.5 μm from the surface, although the scaling is not linear. These results are consistent with the observations of Winet *et al.* (1984) who reported the highest cell concentrations at 10–20 μm from the surface. Stable swimming occurs with a small angle of inclination away from the surface of less than 0.5°. The equilibrium inclination angle varies with wavenumber and decays rapidly approaching the minimal values of k for which accumulation occurs.

Cells swimming with lower wavenumbers are predicted to escape from the surface. The mechanism by which this occurs is unclear, but we note that the extrapolated inclination angle for cells at the minimal values of k for which accumulation occurs is approximately zero, suggesting that the stable swimming configuration degenerates below such values of k.

'Finite distance' surface trapping does not require specialized beating with non-planar components to push the cell towards the surface. Additionally, cells exhibiting rolling motility due to elliptical helicoid beating, as has been inferred from observations of human sperm, exhibited similar accumulation behaviour. The accumulation phenomenon was found to depend on initial angle of inclination. If a cell approaches a surface from a distance of one body length and with a 4°–6° angle of inclination, the cell will be deflected. Similar results were predicted for a planar beating cell. We also found that rolling cells exhibited similar dependence on wavenumber, with $k = 2\pi$ and $k = 4\pi$ producing escape and accumulation respectively.

Such surface trapping is a relatively weak effect, which may be consistent with the observations of Winet *et al.* (1984) and Rothschild (1963) that cells are found in a 'distribution' of swimming heights rather than concentrated exclusively near the surface. Variations in wavenumber between cells will lead to variations in stable accumulation height, which may also be an important factor in producing a distribution of heights. For larger angles of inclination, collision with the surface is predicted to occur, and further simulation within the present framework is not possible. The principle difficulties are that the residuals on the head are unacceptably large as it approaches the surface, and the slender body theory model additionally will break down as the condition $r_3 \ll y_3$ is violated. Nevertheless, our simulations suggest that cells approaching with sufficiently steep angle may align with the 'swept conical envelope' aligned against the surface, as suggested by Woolley (2003) for chinchilla sperm.

We also investigated the possibility of cells with a small angle of inclination between the head plane of flattening and the beat plane, 'gliding' along a surface at a small distance, as reported in mouse sperm, within the context of the human sperm model. Simulations with initial height of $0.03L$–$0.05L$, equivalent to approximately 1.5–3 μm, predicted that such cells were not able to glide in this manner, and indeed cells initially close to a surface will turn away and escape, with or without there being inclination between the head and beat plane. Further clarification of the fluid dynamics of such gliding motion is necessary, and it is possible that features of the head geometry or

subtle aspects of the flagellar beat in species such as the mouse may explain how stable swimming can occur with the head in close proximity to the surface. As noted by Woolley (2003), it is also likely that near the surface the flagellar beat would be modified, which may prevent collision. It may also be that case that trapping occurs after cells collide with the surface, which we cannot simulate with the present framework.

Swimming at finite height so that the cell is not in contact with the surface, but rather is guided to follow it, may have implications for cell function in certain physiological situations. The variation in wavenumber that occurs with changes in viscosity may hence also have an important effect on the swimming height of cells, which may be relevant considering the effect of *in vivo* variations in viscosity along the female reproductive tract and during the menstrual cycle.

The simulation model was also used to test the cell rolling and head trajectory that would occur due to elliptical helicoid beating. The head is predicted to roll by approximately 240° during one beat cycle and traces out a path which appears as consisting of three 'loops' viewed from the front, much like that observed in the slightly different situation of cells swimming against a coverslip by Woolley (2003). Elliptical helicoid beating with a conical envelope results in a non-constant torque exerted by the flagellum on the fluid during the flagellar beat. The flagellar torque, which must be balanced by rolling of the entire cell, has two maxima during each flagellar beat cycle, which causes two periods of high rolling rate, resulting in the 'loops' observed.

In a Newtonian model of flagellar propulsion with prescribed beat pattern and frequency, viscosity does not have any effect on the swimming behaviour predicted. It is known from experiments (see for example Ishijima *et al.* 1986) that viscosity has important effects on beat pattern and frequency; therefore theoretical predictions regarding swimming velocity and trajectory in different viscosity liquids must either make use of beat pattern and frequency parameters that are appropriate to the liquid in question or alternatively model the internal mechanics of the flagellum and the fluid-structure interaction that modifies the flagellum movement (see for example Dillon *et al.* 2007).

Our model does not include the effect of Brownian motion. For sperm cells, which have length of approximately 50 μm, neither translational nor rotational Brownian motion appears to be important in experiments (unpublished observations). However for *Rhodobacter sphaeroides*, a bacterium with a micron-sized body and a flagellum of less than 10 μm, Brownian fluctuations appear to govern cell reorientation during the intermittent stops of its flagellum (Armitage & Macnab 1987). This suggests that rotational Brownian motion may significantly perturb such small cells, which in turn may destabilize the swimming trajectory if the sensitivity to angle of inclination observed here is inherited by the helical flagellar motility of bacteria.

Surface accumulation of sperm is, as indicated by Woolley (2003), a complex phenomenon which depends on flagellar beat pattern and possibly aspects of head geometry. Our findings are summarized below.

(i) We predict that planar beating human sperm cells with planar waveform and wavenumber $k = 3\pi$ perform 'finite distance' surface accumulation; that is they swim stably at a distance of approximately 17 μm from a surface, with approximately 0.4° inclination towards the surface.

(ii) Specialized non-planar components of the beat pattern are not necessary for this accumulation to occur, although cells performing non-planar 'elliptical helicoid' flagellar beating behave similarly.

(iii) The attraction effect is relatively weak, so that cells initially one body length away from the surface and with angle of inclination of up to 2° towards the surface will be trapped; however cells swimming with steeper angles of inclination will be deflected or will approach so closely that simulation will no longer be possible.

(iv) The flagellar wavenumber has a significant effect on the rate of convergence of the trajectory and the eventual stable swimming height, with an increase from $k = 3\pi$ to $k = 4\pi$ resulting in an approximate halving of the stable swimming height, although the relationship is not linear.

(v) Sperm performing rolling motility with conical flagellar envelope and sufficient angle of attack towards the surface may align in the manner reported in chinchilla sperm.

(vi) We predict that human sperm would not be able to perform the 'hydrofoil' surface accumulation reported in mouse sperm for separation distances of 0.03–0.05 body lengths. Consideration of subtle features of the head and flagellum may be required to explain the effect in murine cells.

6. Future work

The hybrid boundary integral/slender body model we have presented has provided insight into the fluid mechanics of cell accumulation at and near surfaces. The model has great potential for the exploration of other aspects of sperm motility, for example the accurate calculation of forces and hence bending moments on the flagellum and their variation due to beat pattern. The model may be adapted to investigate other cell types including the sperm of other species, bacteria and a great many types of cells which use flagella for motility or feeding (see for example Orme, Blake & Otto 2001). The hybrid boundary integral/slender body framework further may be invaluable in the modelling of systems in which flagella and cilia beat near non-planar boundaries, for example the nodal cavity of the embryo (Smith *et al.* 2007; Smith, Blake & Gaffney 2008).

At present we have only simulated one isolated cell near a surface. As discussed in Lighthill (1996*a*), the velocity field around a free-swimming cell decays as a stresslet, with $O(1/r^2)$. In the presence of a surface, which will induce a leading-order image stresslet, this will become $O(1/r^3)$, implying that the hydrodynamic effect of a motile cell close to a surface is relatively short-range. Nevertheless, in both the early stages of *in vivo* migration and in laboratory tests, cells will occur in high concentrations – for example in a wet preparation of undiluted semen, cells will be at such high concentrations that apparent collisions and crossing of paths will occur frequently, and in such situations hydrodynamic interactions will be important. Simulation of multiple cells using the algorithm described in this paper would involve the solution at each time step of linear problems with $N = 3(N^h + N^t + 2)N^{cells}$ degrees of freedom. For a single cell, the matrix set-up and solution are approximately equally expensive. However, the cost of matrix set-up is proportional to N^2, whereas solving linear problems directly is proportional to N^3, and so the use of efficient parallelized iterative solvers may become necessary. However, the $O(1/r^3)$ screening effect would mean that relatively few cells would have to be simulated in order to give insight into the likely behaviour of a single cell in a highly concentrated suspension. It is also likely that simplified models which preserve the essential propulsive/drag effect of each cell, the slender body nature of the flagellum and the image systems in the boundary may give useful insight into the fundamental mechanics of the accumulation effect on individual and multiple cells.

At present, we are working to quantify the three-dimensional beat pattern of human sperm in the presence of a nearby surface. As indicated by Woolley (2003), it is likely that the presence of the surface may suppress the three-dimensional nature of the beat to some extent. As such data become available for human sperm, this model will be used to understand the fluid mechanics of the resulting cell motion. The swimming of sperm in viscoelastic liquids was considered in the initial study of Fulford *et al.* (1998) on the effect of elasticity, subject to the assumption of small-amplitude beating. Cervical mucus has been shown to be viscoelastic (Wolf *et al.* 1977), and extension of the slender body modelling technique to investigate linear viscoelastic effects with finite amplitude beating will also be a subject for future work.

DJS acknowledges the MRC for a training fellowship in computational biology and the Wellcome Trust for a 'Value in People' fellowship. The authors acknowledge invaluable comments from Mr P. Wakeley and Dr D. Loghin of the School of Mathematics along with the members of the reproductive biology research groups in the Schools of Medicine and Biosciences at the University of Birmingham, Mr H. Shum and Mr H. Gadêlha of the Mathematical Institute, University of Oxford, and Dr N. Kapur of the School of Mechanical Engineering, University of Leeds.

Appendix. The flagellar beat pattern

A.1. *Mathematical framework*

We discuss below the mathematical details of the specification of the flagellar beat cycle. In Dresdner & Katz (1981), the flagellum is defined by a curve

$$\xi_2'' = y(\xi_1'', t) \quad \left(0 < \xi_1'' < \xi_1^{max}\right), \tag{A1}$$

where ξ_1^{max} is determined by specifying a constant total flagellar arclength. The curve $\boldsymbol{\xi}''(\xi_1'') = (\xi_1'', \xi_2'', 0)$ defines a planar wave. This must then be translated and rotated to give the body frame position vector $\boldsymbol{\xi}'(\xi_1') = (\xi_1', \xi_2', 0)$, which satisfies (*a*) $\boldsymbol{\xi}'(0) = 0$ and (*b*) that the tangent to $\boldsymbol{\xi}'$ at $\xi_1' = 0$ is $(1, 0, 0)$. This corresponds to the flagellum joining the head at the body frame origin, the flagellum being tangential to the head centreline, as shown in figure 2(*a*). As described in the text, the laboratory frame position vector of the flagellum is given by $\boldsymbol{\xi} = \boldsymbol{X}_0 + \boldsymbol{B} \cdot \boldsymbol{\xi}'$.

In order to discretize the flagellum into collocation points at arclengths $s_q = (q - 0.5)/N^t$ $(q = 1, \ldots, N^t)$ we follow Dresdner & Katz (1981) and consider the arclength function

$$s(\xi_1'', t) = \int_0^{\xi_1''} \left(1 + \left[\frac{\partial y}{\partial x}(x, t)\right]^2\right)^{1/2} \mathrm{d}x. \tag{A2}$$

We invert this function by Newton's method to calculate the position vectors of the collocation points $\boldsymbol{\xi}''(s_q, t)$, corresponding to fixed arclength values. Additionally we distribute quadrature nodes equally along each sub-interval of the flagellum. Since the flagellar patterns considered are periodic, the calculation is carried out for one beat cycle, with $t = 0, \delta t, \ldots, T$.

A.2. *Flagellar waveform of Dresdner & Katz (1981) with variable wavenumber*

For planar beating sperm of various species and in various activation states, Dresdner & Katz (1981) used the general parametrization

$$\xi_2'' = b(\xi_1'')\sin\left(2\pi\left[\frac{\xi_1''}{\lambda(\xi_1'')} - ft\right]\right). \tag{A3}$$

For human sperm in semen, the amplitude and wavelength were chosen as $b(\xi_1'') = 0.1087\xi_1'' + 0.0543$ and $\lambda(\xi_1'') = 1$. In this paper we used the following form:

$$\xi_2'' = b(\xi_1'')\sin(k\xi_1'' - t), \tag{A4}$$

where ξ_1'', ξ_2'' are non-dimensional coordinates, scaled with respect to flagellar length; k is angular wavenumber scaled with respect to the inverse of flagellar length; and t is non-dimensional time, scaled so that $t = 2\pi$ represents one beat cycle. For the original parameterization of Dresdner & Katz (1981), $k = 2\pi$, although in this study we examined values of k from π to 4π. We calculate the velocity components of the flagellum collocation points slightly differently from Dresdner & Katz (1981): we use numerical centred differences to take the time derivatives of the points $\boldsymbol{\xi}'(s_q, t)$.

A.3. *Elementary models of elliptical helicoid and planar sinusoid beating*

Rikmenspoel (1965) and Ishijima *et al.* (1986, 1992) argued respectively that bull and human sperm exhibit an 'elliptical helicoid' beat pattern, that is a beat pattern which is a left-handed helix with elliptical cross-section. For human sperm, the major:minor axis ratio was given by Ishijima *et al.* (1986) as 5 : 1. We formulate an elementary model of this as follows:

$$\xi_2' = \alpha_2\xi_1'\cos(k\xi_1' - t), \quad \xi_3' = -\alpha_3\xi_1'\sin(k\xi_1' - t), \tag{A5}$$

where the amplitude parameters are chosen so that $\alpha_3/\alpha_2 = 0.2$, and we have non-dimensionalized ξ_i' and t as above. This beat pattern will cause cell rolling, as generally observed in motile human sperm in low viscosity medium, which occurs because of the torques associated with the rotating helicoid. We also formulate a corresponding planar beat pattern by simply setting $\alpha_3 = 0$.

REFERENCES

Armitage, J. P. & Macnab, R. M. 1987 Unidirectional, intermittent rotation of the flagellum of rhodobacter sphaeroides. *J. Bacteriol.* **169** (2), 514–518.

Baltz, J. M., Katz, D. F. & Cone, R. A. 1988 Mechanics of sperm–egg interaction at the zona pellucida. *Biophys. J.* **54**, 643–654.

Blake, J. R. 1971 A note on the image system for a stokeslet in a no slip boundary. *Proc. Camb. Phil. Soc.* **70**, 303–310.

Blake, J. R. & Chwang, A. T. 1974 Fundamental singularities of viscous flow. Part 1. Image systems in the vicinity of a stationary no-slip boundary. *J. Engng Math.* **8**, 23–29.

Brokaw, C. J. 1965 Non-sinusoidal bending waves of sperm flagella. *J. Exp. Biol.* **43**, 155–169.

Brokaw, C. J. 1970 Bending moments in free-swimming flagella. *J. Exp. Biol.* **53**, 445–464.

Brokaw, C. J. 1972 Computer simulation of flagellar movement I. Demonstration of stable bend propagation and bend initiation by a sliding filament model. *Biophys. J.* **12**, 564–586.

Brokaw, C. J. 1985 Computer simulation of flagellar movement VI. Simple curvature-controlled models are incompletely specified. *Cell Motil. Cytoskel.* **48**, 633–642.

Brokaw, C. J. 2002 Computer simulation of flagellar movement VII. Coordination of dynein by local curvature control can generate helical bending waves. *Cell Motil. Cytoskel.* **53**, 102–124.

Chwang, A. T. & Wu, T. Y. 1971 A note on the helical movement of micro-organisms. *Proc. R. Soc. Lond.* B **178** (1052), 327–346.

Chwang, A. T. & Wu, T. Y. 1975 Hydrodynamics of the low-Reynolds-number flows. Part 2. The singularity method for Stokes flows. *J. Fluid Mech.* **67**, 787–815.

Clarke, R. J., Jensen, O. E., Billingham, J. & Williams, P. M. 2006 Three-dimensional flow due to a microcantilever oscillating near a wall: an unsteady slender-body analysis. *Proc. R. Soc.* A **462**, 913–933.

Cortez, R. 2001 The method of regularized stokeslets. *SIAM J. Sci. Comput.* **23** (4), 1204–1225.

Cortez, R., Fauci, L. & Medovikov, A. 2005 The method of regularized stokeslets in three dimensions: Analysis, validation and application to helical swimming. *Phys. Fluids* **17** (031504), 1–14.

Cosson, J., Huitorel, P. & Gagnon, C. 2003 How spermatozoa come to be confined to surfaces. *Cell Motil. Cytoskel.* **54**, 56–63.

Cox, R. G. 1970 The motion of long slender bodies in a viscous fluid. Part 1. General theory. *J. Fluid Mech.* **44**, 791–810.

Dillon, R. H., Fauci, L. J., Omoto, C. & Yang, X. 2007 Fluid dynamic models of flagellar and ciliary beating. *Ann. N. Y. Acad. Sci.* **1101**, 494–505.

Dresdner, R. D. & Katz, D. F. 1981 Relationships of mammalian sperm motility and morphology to hydrodynamic aspects of cell function. *Biol. Reprod.* **25**, 920–930.

Dresdner, R. D., Katz, D. F. & Berger, S. A. 1980 The propulsion by large amplitude waves of uniflagellar micro-organisms of finite length. *J. Fluid Mech.* **97**, 591–621.

Drobnis, E. Z., Yudin, A. I., Cherr, G. N. & Katz, D. F. 1988 Hamster sperm penetration of the zona pellucida: kinematic analysis and mechanical implications. *Dev. Biol.* **130** (1), 311–323.

Fauci, L. & McDonald, A. 1995 Sperm motility in the presence of boundaries. *Bull. Math. Biol.* **57** (5), 679–699.

Fulford, G. R., Katz, D. F. & Powell, R. L. 1998 Swimming of spermatozoa in a linear viscoelastic fluid. *Biorheology* **35** (4–5), 295–309.

Gray, J. 1953 Undulatory propulsion. *Quart. J. Microsc. Sci.* **94** (4), 551–578.

Gray, J. 1955 The movement of sea urchin spermatozoa. *J. Exp. Biol.* **32**(4), 775–801.

Gray, J. & Hancock, G. J. 1955 The propulsion of sea-urchin spermatozoa. *J. Exp. Biol.* **32** (4), 802–814.

Gueron, S. & Levit-Gurevich, K. 2001 A three-dimensional model for ciliary motion based on the internal 9+2 structure. *Proc. R. Soc. Lond.* B **268**, 599–607.

Gueron, S. & Liron, N. 1992 Ciliary motion modeling, and dynamic multicilia interactions. *Biophys. J.* **63**, 1045–1058.

Gueron, S. & Liron, N. 1993 Simulations of three-dimensional ciliary beats and cilia interactions. *Biophys. J.* **65**, 499–507.

Hancock, G. J. 1953 The self-propulsion of microscopic organisms through liquids. *Proc. R. Soc.* B **217**, 96–121.

Higdon, J. J. L. 1979*a* A hydrodynamic analysis of flagellar propulsion. *J. Fluid Mech.* **90**, 685–711.

Higdon, J. J. L. 1979*b* The hydrodynamics of flagellar propulsion: helical waves. *J. Fluid Mech.* **94** (2), 331–351.

Hines, M. & Blum, J. J. 1978 Bend propagation in flagella. I. Derivation of equations of motion and their simulation. *Biophys. J.* **23** (2), 41–57.

Hines, M. & Blum, J. J. 1983 Three-dimensional mechanics of eukaryotic flagella. *Biophys. J.* **41**, 67–79.

Ishijima, S., Hamaguchi, M. S., Naruse, M., Ishijima, S. A. & Hamaguchi, Y. 1992 Rotational movement of a spermatozoon about its long axis. *J. Exp. Biol.* **163**, 15–31.

Ishijima, S., Oshio, S. & Mohri, H. 1986 Flagellar movement of human spermatozoa. *Gamete Res.* **13**, 185–197.

Johnson, R. E. 1977 Slender body theory for stokes flow and flagellar hydrodynamics. PhD thesis, California Institute of Technology.

Johnson, R. E. 1980 An improved slender-body theory for Stokes flow. *J. Fluid Mech.* **99** (2), 411–431.

Johnson, R. E. & Brokaw, C. J. 1979 A comparison between resistive-force theory and slender-body theory. *Biophys. J.* **25** (1), 113–127.

Katz, D. F., Blake, J. R. & Pavieri-Fontana, S. L. 1975 On the movement of slender bodies near plane boundaries at low Reynolds number. *J. Fluid Mech.* **72** (3), 529–540.

Katz, D. F., Overstreet, J. W., Samuels, S. J., Niswander, P. W., Bloom, T. D. & Lewis, E. L. 1986 Morphometric analysis of spermatozoa in the assessment of human male infertility. *J. Androl.* **7** (4), 203–210.

Kinukawa, M., Ohmuro, J., Baba, S. A., Murashige, S., Okuno, M., Nagata, M. & Aoki, F. 2005 Analysis of flagellar bending in hamster spermatozoa: characterisation of an effective stroke. *Biol. Reprod.* **73** (6), 1269–1274.

Lauga, E. 2007 Propulsion in a viscoelastic fluid. *Phys. Fluids* **19**, 083104.

Lauga, E., DiLuzio, W. R., Whitesides, G. M. & Stone, H. A. 2006 Swimming in circles: motion of bacteria near solid boundaries. *Biophys. J.* **90** (2), 400–412.

Lighthill, M. J. 1975 Mathematical biofluiddynamics. In *SIAM Regional Conference Series in Applied Mathematics*, Society for Industrial and Applied Mathematics, Philadelphia.

Lighthill, M. J. 1976 Flagellar hydrodynamics. The Jon von Neumann lecture. *SIAM Rev.* **18** (2), 161–230.

Lighthill, M. J. 1996*a* Helical distributions of stokeslets. *J. Engng Math.* **30** (1–2), 35–78.

Lighthill, M. J. 1996*b* Reinterpreting the basic theorem of flagellar hydrodynamics. *J. Engng Math.* **30** (1–2), 25–34.

Liron, N. 2001 The LGL (Lighthill–Gueron–Liron) Theorem–historical perspective and critique. *Math. Methods Appl. Sci.* **24**, 1533–1540.

Liron, N. & Mochon, S. 1976 The discrete-cilia approach to propulsion of ciliated micro-organisms. *J. Fluid Mech.* **75**, 593–607.

Machin, K. E. 1958 Wave propagation along flagella. *J. Exp. Biol.* **35** (4), 796–806.

Machin, K. E. 1963 The control and synchronisation of flagellar movement. *Proc. R. Soc. Lond.* B **158** (970), 88–104.

O'Neill, M. E. & Stewartson, K. 1967 On the slow motion of a sphere parallel to a nearby wall. *J. Fluid Mech.* **27**, 705–724.

Orme, B. A. A., Blake, J. R. & Otto, S. R. 2001 Modelling the motion of particles around choanoflagellates. *J. Fluid Mech.* **475**, 333–355.

Oseen, C. W. 1927 *Hydrodynamik*. Leipzig Akademie Verlag.

Phan-Thien, N., Tran-Cong, T. & Ramia, M. 1987 A boundary-element analysis of flagellar propulsion. *J. Fluid Mech.* **185**, 533–549.

Pironneau, O. & Katz, D. F. 1974 Optimal swimming of flagellated micro-organisms. *J. Fluid Mech.* **66**, 391–415.

Pozrikidis, C. 2002 *A Practical Guide to Boundary-Element Methods with the Software Library BEMLIB*. Chapman and Hall/CRC.

Ramia, M., Tullock, D. L. & Phan-Thien, N. 1993 The role of hydrodynamic interaction in the locomotion of microorganisms. *Biophys. J.* **65**, 755–778.

Rikmenspoel, R. 1965 The tail movement of bull spermatozoa. Observations and model calculations. *Biophys. J.* **5**, 365–392.

Rothschild, L. 1963 Non-random distribution of bull spermatozoa in a drop of sperm suspension. *Nature* **198** (1221–1222).

Russel, W. B., Hinch, E. J., Leal, L. G. & Tieffenbruck, G. 1977 Rods falling near a vertical wall. *J. Fluid Mech.* **83** (2), 273–287.

Shen, J. S., Tam, P. Y., Shack, W. J. & Lardner, T. J. 1975 Large amplitude motion of self-propelling slender filaments at low Reynolds numbers. *J. Biomech.* **8**, 229–236.

Smith, D. J., Blake, J. R. & Gaffney, E. A. 2008 Fluid mechanics of nodal flow due to embryonic primary cilia. *J. R. Soc. Interface* **5**, 567–573.

Smith, D. J., Gaffney, E. A. & Blake, J. R. 2007 Discrete cilia modelling with singularity distributions: application to the embryonic node and the airway surface liquid. *Bull. Math. Biol.* **69** (5), 1477–1510.

Taylor, G. I. 1951 Analysis of the swimming of microscopic organisms. *Proc. R. Soc. Lond. Ser.* A **209**, 447–461.

Taylor, G. I. 1952 The action of waving cylindrical tails in propelling microscopic organisms. *Proc. R. Soc. Lond. Ser.* A **211** (1105), 225–239.

Vernon, G. G. & Woolley, D. M. 1999 Three dimensional motion of avian spermatozoa. *Cell Motil. Cytoskel.* **42**, 149–161.

Vigeant, M. A. S., Ford, R. M., Wagner, M. & Tamm, L. K. 2002 Reversible and irreversible adhesion of motile escherichia coli cells analyzed by total internal reflection aqueous fluorescence microscopy. *Appl. Environ. Microbiol.* **68** (6), 2794–2801.

Winet, H., Bernstein, G. S. & Head, J. 1984 Observations on the response of human spermatozoa to gravity, boundaries and fluid shear. *Reproduction* **70**, 511–523.

Wolf, D. P., Blasco, L., Khan, M. A. & Litt, M. 1977 Human cervical mucus. I. Rheologic characteristics. *Fertil. Steril.* **28** (1), 41–46.

Woolley, D. M. 1977 Evidence for 'twisted plane' undulations in golden hamster sperm tails. *J. Cell Biol.* **75**, 851–865.

Woolley, D. M. 2003 Motility of spermatozoa at surfaces. *Reproduction* **126**, 259–270.

Woolley, D. M. & Vernon, G. G. 2001 A study of helical and planar waves on sea-urchin sperm flagella, with a theory of how they are generated. *J. Exp. Biol.* **204**, 1333–1345.